Cell Reports
Medicine

Article

SOX4-ZIP14-zinc metabolism mediates oncogenesis and suppresses T cell immunity in nasopharyngeal carcinoma

Graphical abstract

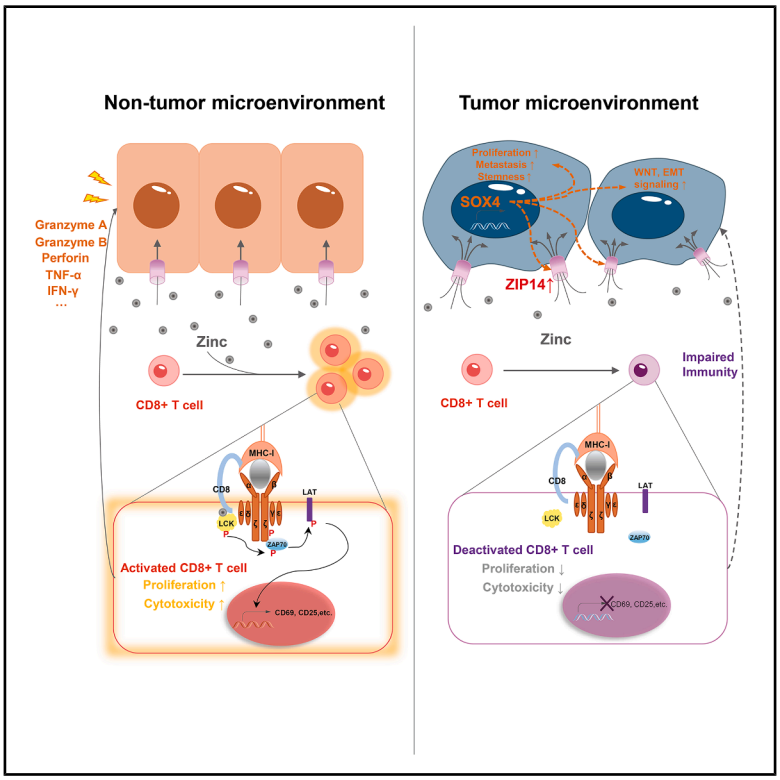

Highlights

- SOX4 is a master transcription regulator in NPC pathogenesis
- NPC cells absorb zinc through the SOX4-ZIP14-zinc axis, enhancing malignant traits
- Microenvironmental zinc deficiency leads to dysfunction of infiltrating CD8$^+$ T cells
- AAV-SOX4-RNAi intratumoral injection inhibits tumor growth and boosts CD8$^+$ T cell response

Authors

Yuma Yang, Qin Liu, Jie Luo, ..., Wei Dai, Lanqi Gong, Xin-Yuan Guan

Correspondence

lqgong94@hku.hk (L.G.),
xyguan@hku.hk (X.-Y.G.)

In brief

Yang et al. demonstrate that nasopharyngeal carcinoma (NPC)-specific SOX4 regulates zinc metabolism via ZIP14, promoting tumor growth and creating a zinc-deficient niche that impairs CD8$^+$ T cell function, highlighting the SOX4-ZIP14-zinc axis as a potential therapeutic target for NPC treatment.

Yang et al., 2025, Cell Reports Medicine 6, 102300
September 16, 2025
https://doi.org/10.1016/j.xcrm.2025.102300

CellPress

Cell Reports Medicine

CellPress
OPEN ACCESS

Article

SOX4-ZIP14-zinc metabolism mediates oncogenesis and suppresses T cell immunity in nasopharyngeal carcinoma

Yuma Yang,[1,2,9] Qin Liu,[1,2,9] Jie Luo,[1,2,9] Ziyang Qi,[1,2] Shanshan Li,[2] Lin Shen,[2] Jishi Li,[2] Xiaona Fang,[3,4] Jiao Huang,[1,2] Beilei Liu,[1,5] Shan Liu,[1,6] Hongyu Zhou,[1,2] Lu Bai,[1,2] Ching Ngar Wong,[1] Baifeng Zhang,[1] Danyang Zheng,[1] Yu Zhang,[3,4,7] Wei Dai,[1,2] Lanqi Gong,[1,2,*] and Xin-Yuan Guan[1,2,4,7,8,10,*]

[1]Department of Clinical Oncology, Li Ka Shing Faculty of Medicine, The University of Hong Kong, Hong Kong SAR, China
[2]Department of Clinical Oncology, The University of Hong Kong-Shenzhen Hospital, Shenzhen, China
[3]Department of Pediatric Oncology, Sun Yat-sen University Cancer Center, Guangzhou, China
[4]State Key Laboratory of Oncology in South China, Collaborative Innovation Center for Cancer Medicine, Sun Yat-sen University Cancer Center, Guangzhou, China
[5]Tung Biomedical Sciences Centre, City University of Hong Kong, Hong Kong SAR, China
[6]Department of Radiation Oncology, Sichuan Clinical Research Center for Cancer, Sichuan Cancer Hospital & Institute, Sichuan Cancer Center, Affiliated Cancer Hospital of University of Electronic Science and Technology of China, Chengdu, China
[7]State Key Laboratory of Oncology in South China, Guangdong Key Laboratory of Nasopharyngeal Carcinoma Diagnosis and Therapy, Sun Yat-sen University Cancer Center, Guangzhou, China
[8]Advanced Energy Science and Technology Guangdong Laboratory, Huizhou, China
[9]These authors contributed equally
[10]Lead contact
*Correspondence: lqgong94@hku.hk (L.G.), xyguan@hku.hk (X.-Y.G.)
https://doi.org/10.1016/j.xcrm.2025.102300

SUMMARY

Subtle variations of micronutrients in the tumor microenvironment often coincide with tumor progression and immune disorders. Nevertheless, the underlying mechanisms of how micronutrients, such as metal ions, influence tumor-intrinsic properties and tumor-immune crosstalk remain inadequately characterized. Here, our integrative analysis of multi-center single-cell, spatial transcriptome sequencing, and bulk RNA sequencing (RNA-seq) cohorts reveals that nasopharyngeal carcinoma (NPC)-specific SRY-box transcription factor 4 (SOX4) governs microenvironmental and cellular zinc metabolism through its downstream target, SLC39A14 (ZIP14), a membrane zinc uptake transporter. Mechanistically, NPC cells enhance zinc uptake and activate Wnt/β-catenin signaling to initiate tumor growth, creating a zinc-deficient niche hostile to T cells. Zinc deficiency of tumor-infiltrating $CD8^+$ T cells impairs LCK phosphorylation and T cell receptor (TCR) signaling, compromising their effector function. Our study elucidates the idea that the SOX4-ZIP14-zinc metabolism axis has a multifactorial effect in NPC, fostering the malignant phenotypes of NPC and suppressing the T cell response through the deprivation of zinc metabolism.

INTRODUCTION

Nasopharyngeal carcinoma (NPC) is a low-incidence malignancy with distinct epidemiological features globally.[1] It is particularly prevalent in Asian and African countries.[2] The etiology of NPC is multifaceted, involving Epstein-Barr virus (EBV) infection, host genetic predispositions, and environmental factors.[3] Although the global incidence of NPC has been declining over the past decade due to population-wide EBV screening, distant metastasis and local recurrence remain the primary causes of treatment failure in patients with NPC.[4] Moreover, the underlying biology contributing to NPC incidence and progression remains largely unexplored. NPC is characterized by a significantly high degree of immune infiltration.[5] These infiltrating immune cells are critical components within the tumor microenvironment (TME) and play a pivotal role in diagnosing and evaluating NPC based on their phenotypic classification and infiltration levels.[5] Despite their proximity to tumor cells within the TME, these immune cells often fail to mount an effective response, suggesting that specific interactions between immune cells and tumor cells might drive immunosuppression. Although immunotherapeutic strategies, particularly immune checkpoint blockade (ICB), have achieved remarkable progress in treating various cancers, only 20%–30% of patients with NPC with high immune infiltration exhibit favorable responses to programmed cell death protein 1 (PD-1) inhibitors combined with chemotherapeutic agents.[6]

Transcription factors (TFs) are crucial regulators that control the expression of target gene networks and maintain normal biological activity by dynamically recognizing and binding to specific DNA regions[7,8]. Based on the structural domains of their

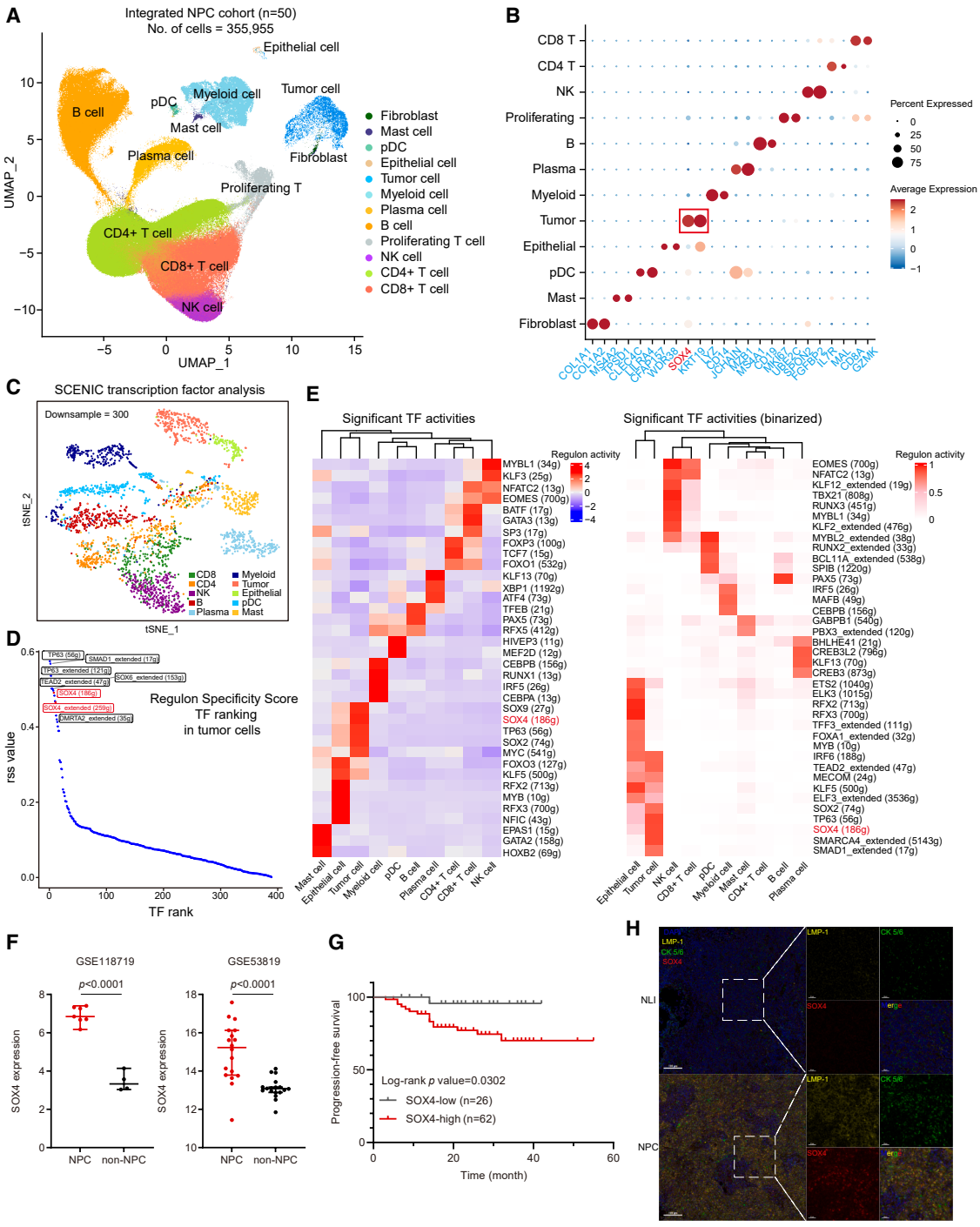

Figure 1. Clinical samples demonstrate a significant expression of SOX4 in NPC

(A) Uniform manifold approximation and projection (UMAP) plot of 355,955 single cells was generated, including 12 subclusters with each color representing one type of cell.

(B) Dotplot showed SOX4 as a signature gene in tumor cluster.

(C) The t-SNE algorithm was applied to the binary regulon activity matrix.

(D) The rank of regulons in NPC cells was determined based on the regulon specificity score (RSS).

(E) SCENIC analysis matched the master regulators with the cell types controlled.

(legend continued on next page)

DNA-binding sites, TFs are categorized into 73 families, with nearly 20% reported to function as oncogenes, playing key roles in the carcinogenesis process.[9]A small subset of TFs, known as ''master transcription factors'' (MTFs), orchestrate gene expression networks and reprogram cell fate.[10]Aberrant activities of MTFs can lead to the abnormal activation or silencing of cellular signaling pathways, regulating various oncogenic processes and contributing to cancer development, progression, metastasis, and recurrence. Recent studies have identified several MTFs as key enablers in distinct cancer types. These TFs regulate crucial processes such as epithelial-mesenchymal transition (EMT),[11] angiogenesis,[12] pro-inflammatory,[13] chemoresistance,[14] metastasis,[15] and other carcinogenic events, whichare highly correlated with poor prognosis and pose significant challenges for clinical treatment. In addition to the uncontrolled phenotypes of tumor cells, cancer progression is frequently accompanied by dysregulation of the immune response. Cellular signaling pathways reprogrammed by MTFs enable tumor cells to remodel immune resistance features and evade immune attacks, whichhave been validated in many cancers.[16–19] While therapeutic strategies targeting MTFs offer a multidimensional therapeutic effect, the mechanisms bywhichMTFs confer immune evasion capabilities to tumor cells in NPC remain poorly understood. To comprehensively investigate how MTFs initiate NPC development within an immune-inflamed microenvironment and acquire resistance to ICB, we established a multi-center single-cell cohort. This cohort comprised 36 primary NPC samples, 10 NPC peripheral blood samples, and 4 nasopharyngeal inflammation samples from three independent studies.[20–22] The findings from single-cell RNA sequencing (scRNA-seq) were further validated using three NPC bulk RNA sequencing (RNA-seq) cohorts[23–25] and our in-house spatial transcriptomics cohort. Analysis from single-cell, spatial, and bulk RNA-seq concurrently revealed the aberrant activities of numerous MTFs in regulating malignant phenotypes, including growth, metastasis, stemness, and immune evasion. Furthermore, these MTF activities were associated with significant defects in $CD8^+$ T cell activation and effector functions. Among all MTFs, we identified SRY-box transcription factor 4 (SOX4) as the most potent driver during NPC pathogenesis. SOX4 has previously been described as a master regulator of cellular EMT process.[26] Many studies have also shown that SOX4 is up-regulated in various cancers and associated with a worse prognosis.[23–25,27–29] In our study, SOX4 was explicitly expressed in more than 80% of NPC cells at single-cell resolution, corresponding to potent regulatory activities in Wnt signaling-dependent tumor initiation and inhibition of T cell receptor (TCR) signaling in $CD8^+$ T cells. We further demonstrated that SOX4 transcriptionally enhanced SLC39A14 (ZIP14) expression, resulting in a higher uptake of free zinc from the TME into NPC cells, whichfueled the activation of Wnt signaling. Concurrently, the microenvironmental zinc deficiency led to $CD8^+$ T cell deactivation by lowering the intracellular zinc level. Epidemiological evidence indicates that metastatic NPC,[30] breast cancer,[31] and colon cancer[32]exhibit elevated zinc levels in malignant tissues.

The roles of zinc transporters in tumor progression are tumor specific and exhibit distinct patterns across different malignancies. In pancreatic cancer, ZIP4 is uniquely overexpressed in tumor cells and promotes tumor progression.[33,34] Conversely, malignant prostate tissue exhibits significantly reduced zinc levels, primarily due to downregulation of ZIP1, leading to decreased intracellular zinc concentrations. This reduction subsequently dysregulates zinc-dependent signaling pathways and facilitates oncogenic activity.[35] In NPC, several studies have reported that ZIP4 can induce EMT and decrease radiosensitivity, thereby promoting NPC progression and impairing therapeutic efficacy.[36–38] Meanwhile, zinc transporters are critical for immune cell function. Previous research has demonstrated that zinc uptake mediated by ZIP10 is essential for B cell development and function.[39,40] ZIP8 plays a vital role in various immune cells related to innate immunity,[41] while ZIP6 is an essential molecule involved in T cell metabolism.[42] Despite extensive research on zinc transporters in human cancers, the functional significance of ZIP14 in NPC has not been previously reported. Our study systematically elucidated how the SOX4-ZIP14 axis disrupts zinc homeostasis between tumor cells and $CD8^+$ T cells, thereby contributing to malignant progression in NPC.

In pre-clinical models of patient-derived xenografts (PDXs), SOX4-targeting adeno-associated virus type 2 vector (AAV-2) gene therapy exhibited a synergistic effect with both chemotherapy and ICB. Notably, the combined use of therapeutic SOX4 inhibition and PD-1 blockade arrested tumor growth and reinvigorated the effector function of intratumoral $CD8^+$ T cells simultaneously. In summary, therapeutic targeting of the SOX4-ZIP14-zinc axis provides a potential strategy and pre-clinical evidence for optimizing the therapeutic efficacy of NPC and overcoming ICB resistance in patients with NPC.

RESULTS

SOX4 is a master transcription regulator in NPC cells

Given the pronounced differences in gene expression patterns between tumor and normal tissues, we first undertook an instructive comparative analysis. As previously described,[20] we generated an extensive scRNA-seq profile by integrating datasets from three independent studies.[20–22] We processed the dataset and clustered a total of 355,955 single cells into major cell lineages (Figure 1A). Among all marker genes in each major cell type, we found that SOX4 was a specific marker up-regulated in most NPC cells (Figures 1B and S1A), significantly co-expressing with the well-known NPC marker KRT19 (Figure S1B). Since SOX4 is a TF, we subsequently inferred a comprehensive TF regulatory network through SCENIC analysis, which predicted TF activities across cell subpopulations (Figure 1C). As anticipated,

(F) Normalized SOX4 expression in two NPC RNA-seq cohorts (two-sided unpaired t test). From left to right: GSE118719 (tumor $n = 7$, normal $n = 4$), GSE53819 (tumor $n = 18$, normal $n = 18$).

(G) The progression-free survival for patients with NPC divided by SOX4 expression from GSE102349 (high $n = 26$, low $n = 62$, two-sided log rank test).

(H) Multi-IF staining of a representative NPC section (bottom) and a nasopharyngeal lymphatic inflammation (NLI) tissue (top) showed co-expression of LMP-1 (yellow), CK 5/6 (green), and SOX4 (red), with nuclei counterstained with DAPI (blue). Scale bars: 100 μm, 20 μm.

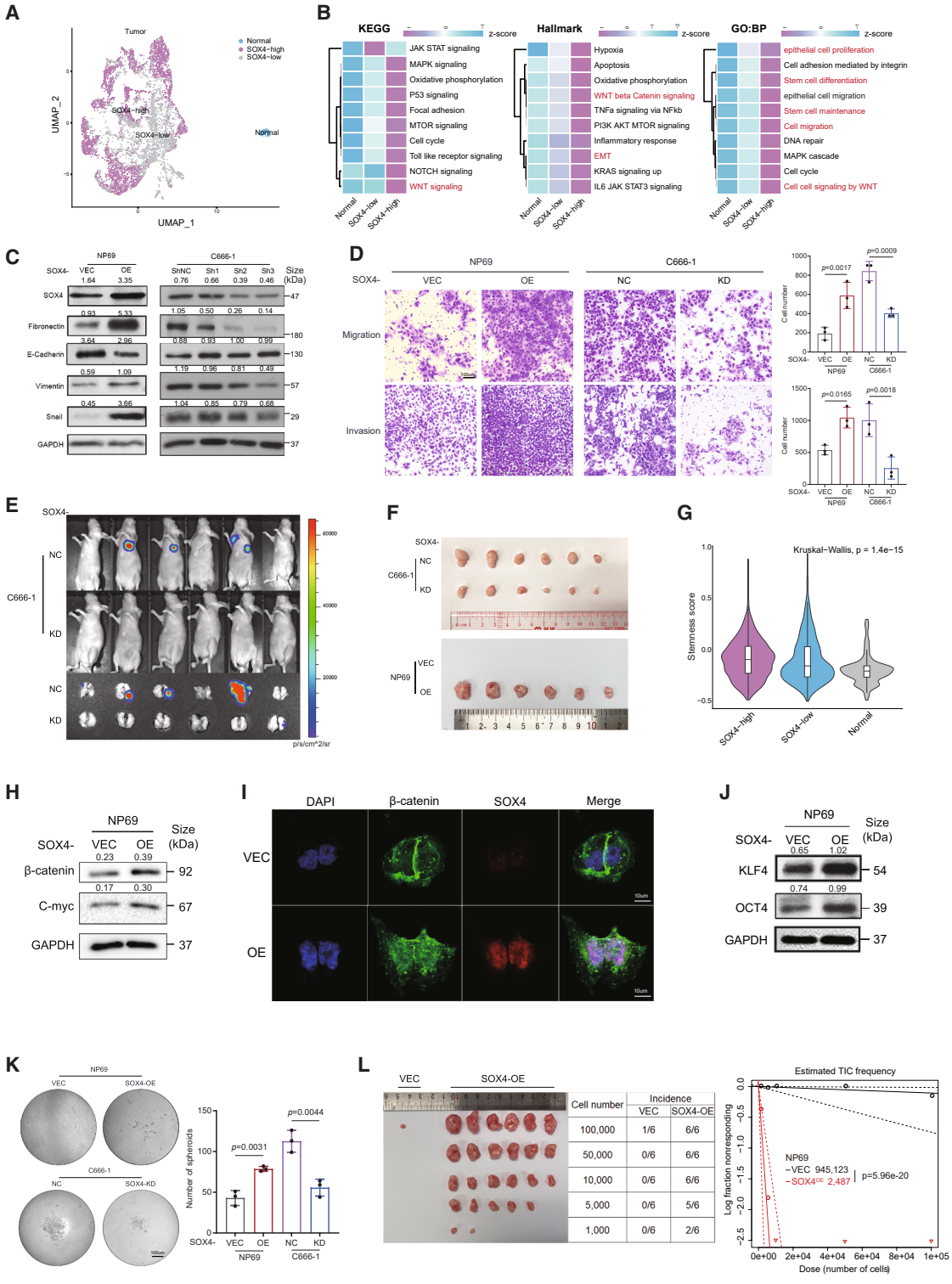

Figure 2. SOX4 regulates intrinsic phenotypes of NPC

(A) A UMAP plot was generated for 7,359 cells, which included 7,266 tumor cells exhibiting high and low expression levels of SOX4 and 93 normal epithelial cells, extracted from patients with NPC and NLI, respectively.

(B) Major signaling pathways and biological activities of the different subtypes were calculated in gene set variation analysis (GSVA) using the "*Z* score" method.

(C) Western blot analysis of SOX4 and EMT markers in NP69 and C666-1 cells transfected with SOX4 and their control group.

(legend continued on next page)

tumor cells displayed distinct TF activities compared to nasopharyngeal epithelial cells. These differentially activated TFs included TP63, SMAD1, TEAD2, SOX6, SOX4, and DMRTA2 (Figures 1D and 1E). We examined the expression pattern of these TFs with top activities and found the restricted expression of SOX4 in both EBV+ and EBV− NPC cells, while the other TFs were sparsely expressed in all cell types (Figure S1C). Furthermore, we analyzed multiple RNA-seq GEO cohorts of clinical samples from NPC and non-cancer patients, which revealed a consistent up-regulation and inferior prognosis effect of SOX4 in NPC (Figures 1F and 1G). Multiplex immunofluorescence staining showed co-localization of SOX4 along with the NPC marker LMP-1 and the squamous carcinoma marker CK5/6, while non-tumor regions showed minimal detection (Figure 1H).

SOX4 confers malignant phenotypes of NPC cells

To investigate the role of SOX4 in regulating the biological processes of NPC cells, we characterized a subset of 7,266 tumor cells and 93 normal nasopharyngeal epithelial cells from the integrated single-cell cohort mentioned previously. The tumor cells were then categorized into high- and low-SOX4 expression groups based on their median SOX4 expression levels (Figure 2A). The SOX4-high tumor cells exhibited more potent oncogenic activities, including the EMT pathway, Wnt signaling, and Hedgehog signaling, which are associated with cell metastasis, stemness, and growth (Figures 2B and S2A).

Next, we established stable SOX4-knockdown (KD) and -overexpression (OE) cells in the NPC cell line C666-1 and the immortalized normal nasopharyngeal epithelial cell line NP69 (described in STAR Methods), respectively, after evaluating the basal SOX4 expression levels in the parental cell lines (Figures S2B and S2C). MTFs are recognized for their role in regulating many biological activities. First, we used immunoblotting to validate that high SOX4 expression could increase fibronectin, vimentin, and Snail, whereas it decreased E-cadherin, suggesting EMT activation (Figure 2C). In the SOX4-KD assays, we selected the SOX4-Sh2 C666-1 cell line for subsequent analysis because it had higher KD efficiency and more apparent phenotypes. Moreover, the metastatic capability, including migration and invasion, of NP69 cells was enhanced by SOX4 OE both *in vitro* and *in vivo*, while SOX4 KD led to the opposite effect in C666-1 cells (Figures 2D, 2E, and S2D). These results collectively indicated that SOX4 could enhance cell invasion and migration via EMT to develop distal metastasis. We also found that increased SOX4 expression augmented the capability of *in vivo* tumor growth and *in vitro* colony formation of NP69 cells (Figures 2F and S2E–S2G), whereas downregulated SOX4 diminished colony formation as shown in foci formation and soft agar assays (Figures S2F and S2G). These results provided experimental evidence of SOX4's role in promoting NPC metastasis and proliferation.

Several SOX family members regulate cancer stemness.[43–47] Using a multivariate linear regression model incorporating reported NPC stemness signatures, including KLF4,[48] CD44,[49] LMP1,[50] FOXM1,[51] LGR5,[52] and OVOL2,[53] we found that SOX4 expression was positively correlated with stemness levels in the single-cell data (Figure 2G). As shown by our previous bioinformatic analysis (Figures 2B and S2A), the elevated expression of SOX4 might suggest the activation of the Wnt/β-catenin pathway. The immunoblotting results validated that NPC cells maintained stemness characteristics through enhanced Wnt/β--catenin transcriptional activity stimulated by SOX4 (Figure 2H). Thus, we identified the nuclear translocation of β-catenin in SOX4-OE cells via immunofluorescence (IF) staining, demonstrating that SOX4 could activate the Wnt pathway (Figure 2I) for regulating NPC stemness. Additionally, stemness-related markers, including KLF4 and OCT4, also exhibited a significant increase after SOX4 OE (Figure 2J). *In vitro* sphere formation assay indicated that SOX4 enhanced the number of cell spheroids, which is an indicator of cancer stemness (Figure 2K). To validate the self-renewal capacity mediated by SOX4, we conducted a limiting dilution tumor formation assay in NOD/SCID mice. Mice injected with SOX4-overexpressed NP69 cells showed a significantly higher tumor incidence, which can be induced by fewer tumor-initiating cells injected (Figure 2L).

SOX4 renders resistance to T cell-mediated cytotoxicity in NPC cells

Besides SOX4's role as an MTF in regulating many intrinsic malignant phenotypes of NPC cells, it might also have an immunoregulatory effect in NPC as many other oncogenic MTFs do. The infiltrating T cells within the NPC microenvironment exhibit characteristics indicative of immune dysfunction.[54] Previous studies have suggested that the functional loss of T cells in the TME is commonly associated with the stemness-like phenotype of tumor cells.[55,56] We hypothesized that SOX4-high NPC cells might contribute to the establishment of an immune-resistant microenvironment for NPC initiation and progression. This was supported by a significant reduction in the effector function of

(D) Stably edited SOX4 affected the migration and invasion ability of NP69 or C666-1 cells *in vitro* by transwell assay (n = 3, 24 h), scale bar: 100 μm.
(E) The NOD/SCID mice were injected with cells suspensions via tail vein for pulmonary metastasis assay (n = 6).
(F) Effect of SOX4 on tumor formation of cells in the subcutaneous implantation NOD/SCID mouse model (n = 6).
(G) Stemness scores were calculated based on single-cell transcriptomes (tumor cells n = 7,266, normal cells n = 93, Kruskal-Wallis test).
(H) The expression levels of β-catenin and c-Myc were quantified by immunoblotting in SOX4-transfected NP69 cells.
(I) Cell immunofluorescence staining presented the activation of the Wnt pathway that β-catenin translocated from the cytoplasm to the nucleus following an increase in SOX4, scale bar: 10 μm.
(J) Overexpression of SOX4 led to an increase of stemness characteristics in NP69 cells observed by western blot.
(K) Representative images demonstrated the capacity for sphere formation in floating cultures, as observed through sphere formation assays (n = 3), scale bar: 100 μm.
(L) *In vivo* extreme limiting dilution assay (ELDA) using NOD/SCID mice (n = 6); limiting dilution plots and stem cell frequencies were calculated using ELDA software (http://bioinf.wehi.edu.au/software/elda/). (C, H, and J) Western blots were quantified using ImageJ. (D–J) The "n" value represents the number of biologically independent samples in each group. The data were presented as mean ± SD and analyzed using a two-sided unpaired t test, unless otherwise specified.

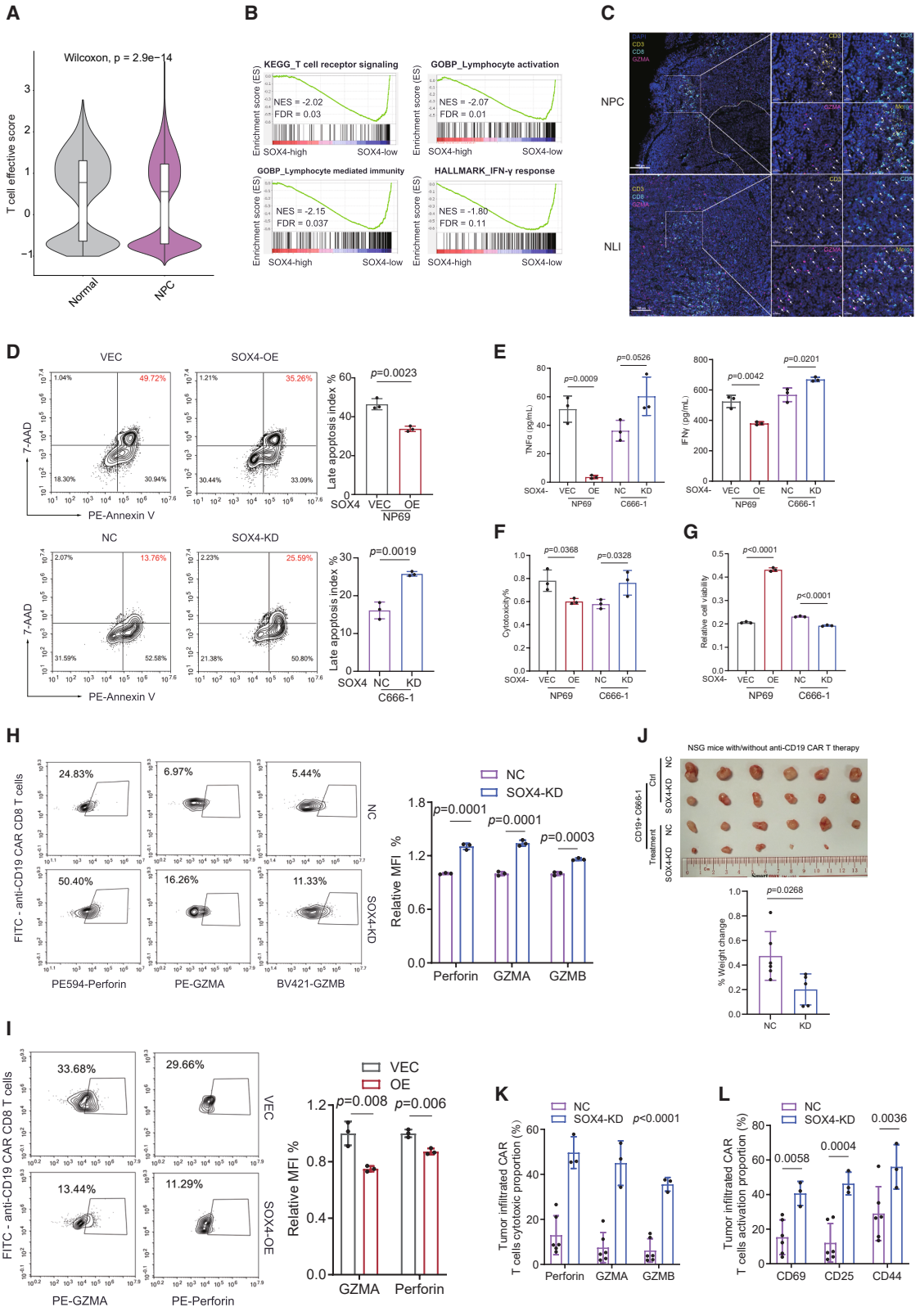

(legend on next page)

$CD8^+$ T cells within NPC tissues, as observed at single-cell resolution (Figure 3A). Gene set enrichment analysis (GSEA) using bulk transcriptomics data revealed that multiple anti-tumor immune pathways, including TCR signaling, interferon-gamma (IFN-γ) response, and lymphocyte-related immunity, were downregulated in SOX4-high tumor tissues (Figure 3B). Furthermore, multicolor immunofluorescence staining of clinical samples demonstrated a higher enrichment of cytotoxic $CD8^+$ T cells in inflammatory tissues compared to NPC tissues (Figure 3C). We then assessed the immune evasion effect by co-culturing $CD8^+$ T cells with C666-1 cells (SOX4-high) and NP69 cells (SOX4-low), respectively, to evaluate the phenotypic and functional changes of $CD8^+$ T cells. Both cell lines were transduced with stable CD19, enabling antigen-specific recognition by $CD8^+$ T cells engineered with an anti-CD19 chimeric antigen receptor (CAR) (Figures S3A–S3C). The viability of target cells in the co-culture system showed stronger resistance to T cell killing in C666-1 cells (Figure S3D). Concurrently, the proportions of granzyme A+ (GZMA) and perforin+ $CD8^+$ T cells markedly declined (Figure S3E). This result suggested that C666-1 cells exhibited greater resistance to $CD8^+$ T cell-mediated cytotoxicity.

Next, we aimed to confirm whether SOX4 was the reliable candidate responsible for enhancing the immune escape of NPC cells. The SOX4-edited C666-1 and NP69 cells were further introduced to CD19 (Figure S3F) and subjected to co-culture assays. The results of co-culture condition settings demonstrated that the most significant differences of both SOX4-OE and KD groups emerged at 24 h with an E:T ratio of 4:1. While cytotoxic effects seem more significant at 48 h (Figure S3G), we selected the 24-h time point for our final co-culture conditions to avoid potential confounding effects from SOX4's intrinsic impact on target cell viability that became pronounced from 48 h, as shown in Figure S2E. Indeed, SOX4-high cells demonstrated a significantly stronger resistance to $CD8^+$ T cell killing (Figure 3D), and the levels of tumor necrosis factor alpha (TNF-α) and IFN-γ secreted by $CD8^+$ T cells also decreased (Figure 3E), consistent with the observed reduction in the populations of GZMA+, GZMB+, and perforin+ $CD8^+$ T cells (Figures 3H and 3I). Additionally, the lactate dehydrogenase (LDH) leakage method (Figure 3F) and the XTT assay (Figure 3G) further indicated higher viability and lower cell death levels of SOX4-high cells, post co-culturing with antigen-specific $CD8^+$ T cells. We also assessed the CD25 and CD69 expression on the co-cultured $CD8^+$ T cells, as this reflected the cytotoxic function initiated by TCR signaling activation. Unsurprisingly, SOX4-high cells were also able to inhibit $CD8^+$ T cell activation (Figures S3H and S3I).

Due to the scarcity of mouse NPC cell lines and spontaneous NPC mouse models for immunology studies, we established an adoptive CAR T transfer model and a peripheral blood mononuclear cell (PBMC)-engrafted humanized mouse model for studying interactions between NPC cells and T cells. To investigate the potential efficacy of CAR T cell therapies for NPC treatment in conjunction with SOX4 suppression, $CD19^+$ NPC-bearing NSG mice were administered a single intravenous dose of anti-CD19-CAR $CD8^+$ T cells. Notable anti-tumor effects were observed in the SOX4-KD tumors, characterized by significant tumor shrinkage (Figure 3J), an increased number of activated $CD8^+$ CAR T cells, and a higher proportion of cytokine-producing $CD8^+$ CAR T cells in the TME (Figures 3K and 3L).

Furthermore, we found that even in an allogenic immune system, the downregulation of SOX4 in NPC cells resulted in tumor suppression (Figure S3J) and significantly enhanced the maintenance of infiltrated $CD8^+$ T cell activation and cytokine production (Figure S3K). GZMA+ $CD8^+$ T cells also exhibited higher infiltration in SOX4-KD tumors, shown by immunohistochemistry staining (Figure S3L). These results further illustrated the role of SOX4 in immunosuppression, not only via an antigen-specific manner but also via an unspecific one.

Overall, our findings demonstrated that SOX4 was a critical MTF that conferred resistance to $CD8^+$ T cell-mediated immunity against NPC. Therapeutic suppression of SOX4 might represent an effective strategy to simultaneously inhibit tumor growth and enhance T cell-mediated immunity.

SOX4 reprograms zinc metabolism in NPC cells by regulating ZIP14

To delineate the underlying mechanism of SOX4 in co-regulating tumorigenicity and immune evasion, we first hypothesized that

Figure 3. SOX4 renders NPC cells resistant to $CD8^+$ T cell-mediated cytotoxicity

(A) The effective score of infiltrated $CD8^+$ T cells was computed at the single-cell level (from tumor n = 55,044, from normal n = 1,988, Wilcoxon test).

(B) The bulk transcriptomic dataset from the GEO database (GSE102349) containing 88 patients with NPC was used to conduct GSEA analysis to calculate the enrichment of immune-related pathways between the SOX4-high and SOX4-low groups (n = 44 in each group).

(C) The distribution and abundance of infiltrated cytotoxic $CD8^+$ T cells were identified by multicolor immunofluorescence in the NPC and NLI clinical specimens, scale bars: 100 μm, 20 μm.

(D–G) In co-culture system of anti-CD19 CAR $CD8^+$ T cells and SOX4-transduced $CD19^+$ cells (E:T = 4:1, duration = 24 h), the apoptosis of target cells was analyzed by flow cytometry (D, n = 3), the concentration of secreted cytokines (IFN-γ and TNF-α) was measured using ELISA (E, n = 3), the release of LDH in the culture medium was quantified with an LDH assay kit (cytotoxicity percentage was calculated followed by the kit manual: percent cytotoxicity = [experimental LDH release − medium background]/[maximum LDH release control − medium background], maximum LDH release control is the maximum LDH release from NPC cell lines without CAR T cells) (F, n = 3), and relative cell viability was assessed through the XTT assay, calculated by cell viability of co-cultured tumor cells normalized to that of tumor cells without CAR T cells (G, n = 3).

(H and I) The fraction of cytotoxic $CD8^+$ T cells post co-culture was analyzed by flow cytometry (n = 3).

(J) An *in vivo* study in subcutaneous implantation of CD19-transfected SOX4-NC and SOX4-KD NPC cells in immunodeficient NSG mice with/without CAR T treatment. Tumors were collected (without CAR T: NC, n = 6; KD, n = 6; with CAR T: NC, n = 6; KD, n = 5). The percentage weight change was calculated by normalizing the tumor weight of the treatment group to that of the corresponding control group.

(K and L) Infiltrated cytotoxic $CD8^+$ T cell fractions (K, NC, n = 6; KD, n = 3) and percentage of activation (L, NC, n = 6; KD, n = 3); the tiny tumor in the KD group with rare $CD8^+$ T cell infiltration was excluded from statistical analysis. The relative MFI was calculated by normalizing the MFI of the gene-edited group to that of the corresponding control group. (D–L) The "n" value represents the number of biologically independent samples in each group. The data were presented as mean ± SD and analyzed using a two-sided unpaired t test, unless otherwise specified.

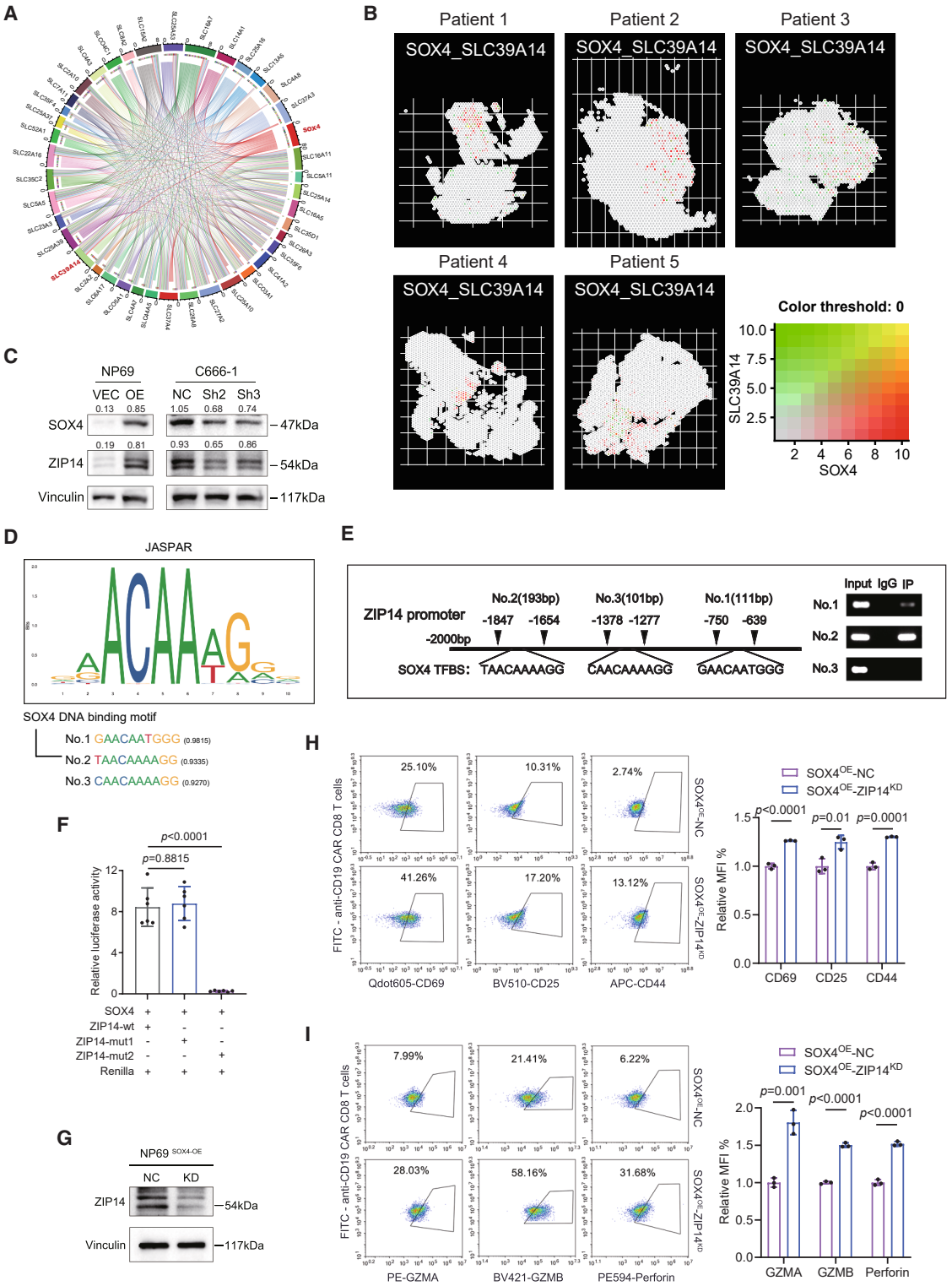

Figure 4. ZIP14 is the downstream target of SOX4 in NPC cells

(A) Chord diagram showed the correlation between SOX4 and measured solute transporter carriers identified by Pearson correlation analysis in bulk RNA-seq data (GSE102349).

(B) Spatial co-localization of SOX4 and ZIP14 (GSE200310).

(C) The protein expression of ZIP14 was determined by western blotting in NP69 and C666-1 cells transfected with SOX4 or a control.

(legend continued on next page)

SOX4 might exert its function via metabolism reprogramming. Tumor cells disrupt the metabolic homeostasis of the TME by utilizing and remodeling metabolites through solute carriers (SLCs),[57] inevitably affecting both tumor cells and infiltrated immune cells. Thus, we evaluated the correlation of SOX4 with SLCs in transcriptomic data, and ZIP14 emerged as one of the most significantly correlated targets (Figure 4A). This strong positive correlation was validated by independent GEO cohorts (Figure S4A). Furthermore, we confirmed the spatial proximity of SOX4 and ZIP14 through our in-house spatial transcriptomics dataset,[54] which consistently demonstrated a significant co-localization between ZIP14 and SOX4 (Figures 4B and S4B).

ZIP14 is a zinc transporter protein primarily responsible for facilitating the transport of extracellular zinc into cells and for participating in cellular metabolism. ZIP14 was found to be up-regulated in patients with NPC (Figure S4C), exhibiting significant accumulation in NPC cells (Figure S4D), and was correlated with a worse prognosis (Figure S4E). We subsequently measured the protein levels (Figure 4C) and mRNA levels (Figure S4F) of ZIP14 in NP69 and C666-1 cells that were transfected with either a SOX4-OE or SOX4-KD plasmid. As predicted, the expression levels of ZIP14 varied in response to SOX4 expression, indicating that ZIP14 was likely to be regulated by SOX4. We utilized JASPAR to predict the binding sites of SOX4 within the promoter region of ZIP14 (Figure 4D; Table S1). Chromatin immunoprecipitation (ChIP)-PCR assays were performed to assess the potential binding sites by using a SOX4-3×FLAG sequence constructed in the CV702 vector (purchased from Shanghai Genechem Co., Ltd.). Three primer pairs around the predicted binding motifs with top three predicted scores were designed to measure DNA enrichment of these fragments. The ChIP-PCR results (Figure 4E) showed that fragments no. 1 and 2 could be directly bound by SOX4, while fragment no. 3 and the negative control failed to be amplified. These two binding sites were then subjected to mutation (Figure S4G) and determined using dual-luciferase reporter experiments. The relative luciferase activity of the construct containing mutant binding site 1 was activated by SOX4 expression, while mutant binding site 2 did not show activation, suggesting that SOX4-mediated activation of ZIP14 expression requires the integrity of binding site no. 2 in the ZIP14 promoter (Figure 4F).

Next, we performed rescue experiments by silencing ZIP14 in SOX4-OE NP69 cells (Figures 4G and S4H). The purpose for ZIP14 KD in SOX4-OE NP69 cells was to determine whether ZIP14 is essential for SOX4-driven tumor phenotype enhancement and immune resistance. Notably, ZIP14 KD significantly impaired NPC cell proliferation and clonogenicity *in vitro* (Figures S4I and S4J), suggesting that ZIP14 significantly diminished the tumorigenic capacity conferred by SOX4. ZIP14 could regulate tumor cell-intrinsic pathways independent of immune modulation. Subsequently, we investigated whether the reduction of ZIP14 could counteract the immune resistance induced by SOX4 OE in the CAR T co-culture system (Figure S4K). Following co-culture, the relative viability of target cells with ZIP14 KD was significantly reduced (Figure S4L). The proportion of activated (Figure 4H) and effector $CD8^+$ T cells (Figure 4I) increased significantly. These results demonstrated that the oncogenic and immunosuppressive effects of SOX4 were primarily mediated through ZIP14.

NPC-specific ZIP14 restrains T cell effector function via competitive zinc deprivation

Previous research has reported that minerals, including calcium, magnesium, potassium, and iron, act as the 4^{th} signal in T cell quiescence and activation.[58] Zinc has also been identified as critical in the TCR signaling pathway.[42] Our previous results demonstrated that the function of $CD8^+$ T cells was restored while ZIP14 was inhibited in NPC cells (Figures 4H and 4I). Single-cell data indicated that the percentage of ZIP14 expression in T cells was significantly lower than in tumor cells (Figure S5A), suggesting that tumor cells may have a competitive edge in acquiring zinc through ZIP14. The enrichment analysis based on single-cell data revealed that zinc metabolism and transport were elevated in NPC cells with high SOX4 expression (Figure 5A), whereas they were diminished in NPC-infiltrated $CD8^+$ T cells (Figure 5B). A validation cohort of the bulk transcriptome dataset confirmed the tumor-enriched GSEA signatures of zinc homeostasis (Figure 5C). The zinc in the culture medium mainly came from fetal bovine serum, with a concentration of approximately 10 μM. To regulate the zinc concentration in the medium for subsequent experiments, we used zinc chelator TPEN at a 1:1 ratio to neutralize and employ zinc chloride to supply. This method effectively regulated intra- and extracellular zinc concentrations (Figures S5B and S5C).

To evaluate the differential effects of zinc on $CD8^+$ T cell activity and tumor cell viability, we measured the half-maximal effective concentration (EC50) for each cell type. Notably, the disparity in EC50 values implied that $CD8^+$ T cells might be more vulnerable to zinc depletion than tumor cells (Figure 5D). To test this speculation, C666-1 cells and activated $CD8^+$ T cells were cultivated together in a transwell device with a 1-μm pore size (Figure S5D). When the zinc concentration fell below (5 μM) the normal concentration (10 μM), there was a significant reduction in $CD8^+$ T cell activation (Figure 5E), while the viability of tumor cells remained above 80% (Figure 5F). When

(D) The top three conservative SOX4-binding sites within the 2,000 bp upstream of the ZIP14 DNA promoter-proximal region were computationally predicted using JASPAR 2024.

(E) ChIP-PCR detection of SOX4 binding motif within ZIP14 promoter region. PCR amplification was carried out with DNA fragments that were immunoprecipitated by anti-FLAG M2 antibody (IP), together with total DNA fragment (input) and DNA fragments that were immunoprecipitated by anti-IgG (IgG).

(F) The two highest predicted binding sites were subjected to mutation and determined using a dual-luciferase reporter assay.

(G) Western blotting was employed to confirm the effective knockdown of the ZIP14 protein in SOX4-overexpressing NP69 cells.

(H and I) The fractions of activated (H, $n = 3$) and cytotoxic (I, $n = 3$) $CD8^+$ T cells were assessed by flow cytometry, respectively. The "*n*" value represents the number of biologically independent samples in each group. The data were presented as mean ± SD and analyzed using a two-sided unpaired t test, unless otherwise specified.

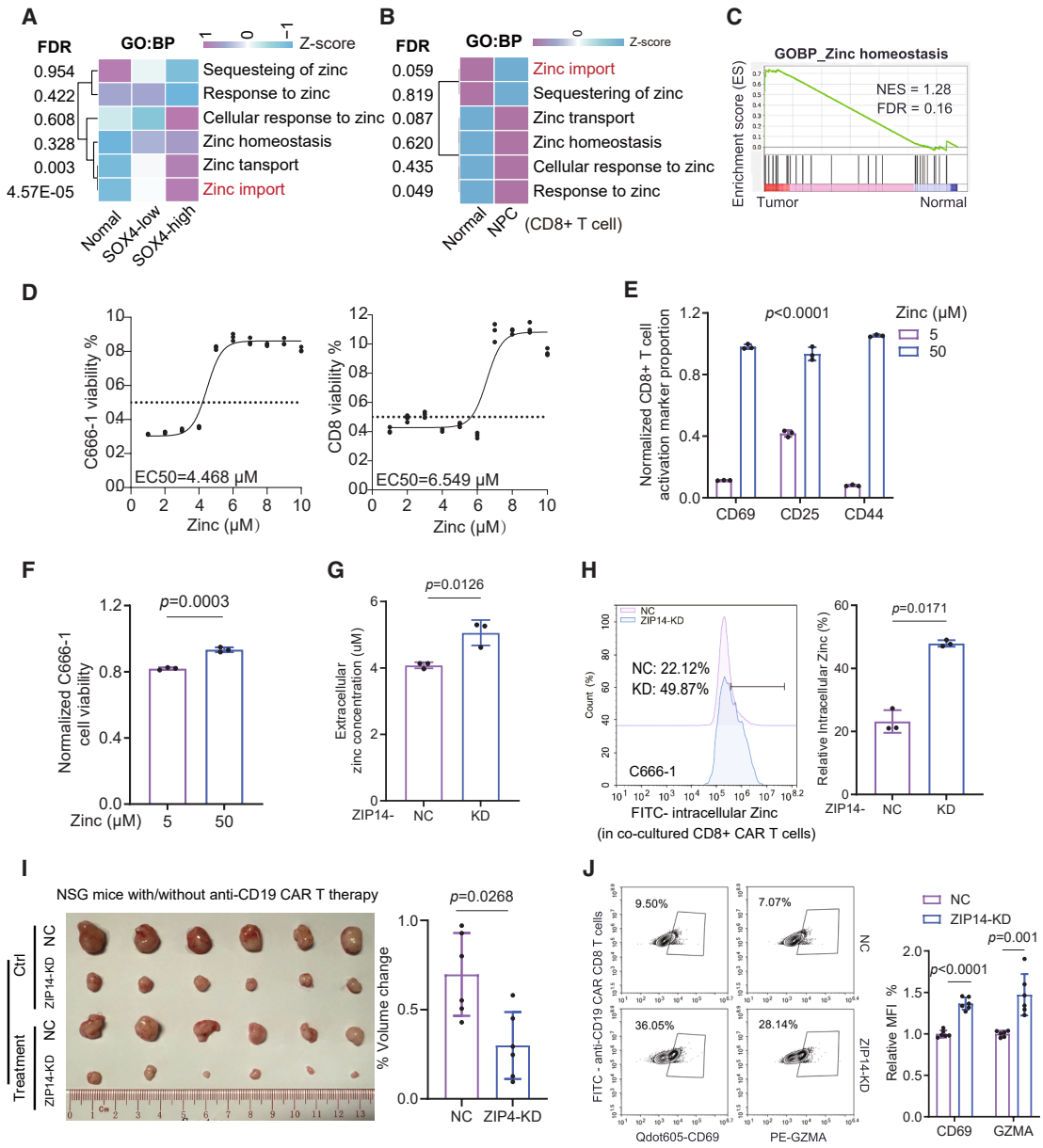

Figure 5. NPC cells compete with CD8 T cells for zinc via ZIP14

(A and B) The GSVA enrichment analysis disclosed an increase in zinc imports in SOX4-high tumor cells (A) and a reduction in zinc import in tumor-derived CD8$^+$ T cells (B).

(C) Validation of zinc homeostasis in NPC and non-NPC patients from the GEO dataset (GSE53819).

(D) The EC50 of zinc to tumor cells (4.468 μM) and CD8$^+$ T cells (6.549 μM) was evaluated by normalized cell viability cultured in the complete medium containing gradient concentration of zinc (XTT, n = 3).

(E and F) Proportion of activated CD8$^+$ T cells (E) and cell viability of C666-1 cells (F) under excess zinc (50 μM) and deficient zinc (5 μM) conditions (n = 3).

(G and H) After 24 h of co-culture with ZIP14-KD cells, extracellular zinc concentration (G) in the culture medium and intracellular zinc concentration (H) of CAR CD8$^+$ T cells were determined using the appropriate zinc assay kits (n = 3).

(I) The ZIP14-NC and ZIP14-KD tumor in immunodeficient NSG mice and anti-CD19 CAR T-engrafted humanized NSG mice (n = 6). The percentage volume change is calculated by normalizing the tumor weight of the treatment group to that of the corresponding control group.

(J) The fractions of tumor-infiltrating activated CD8$^+$ T cells and effector CD8$^+$ T cells were analyzed using flow cytometry. (D–J) The "n" value represents the number of biologically independent samples in each group. The data were presented as mean ± SD and analyzed using a two-sided unpaired t test.

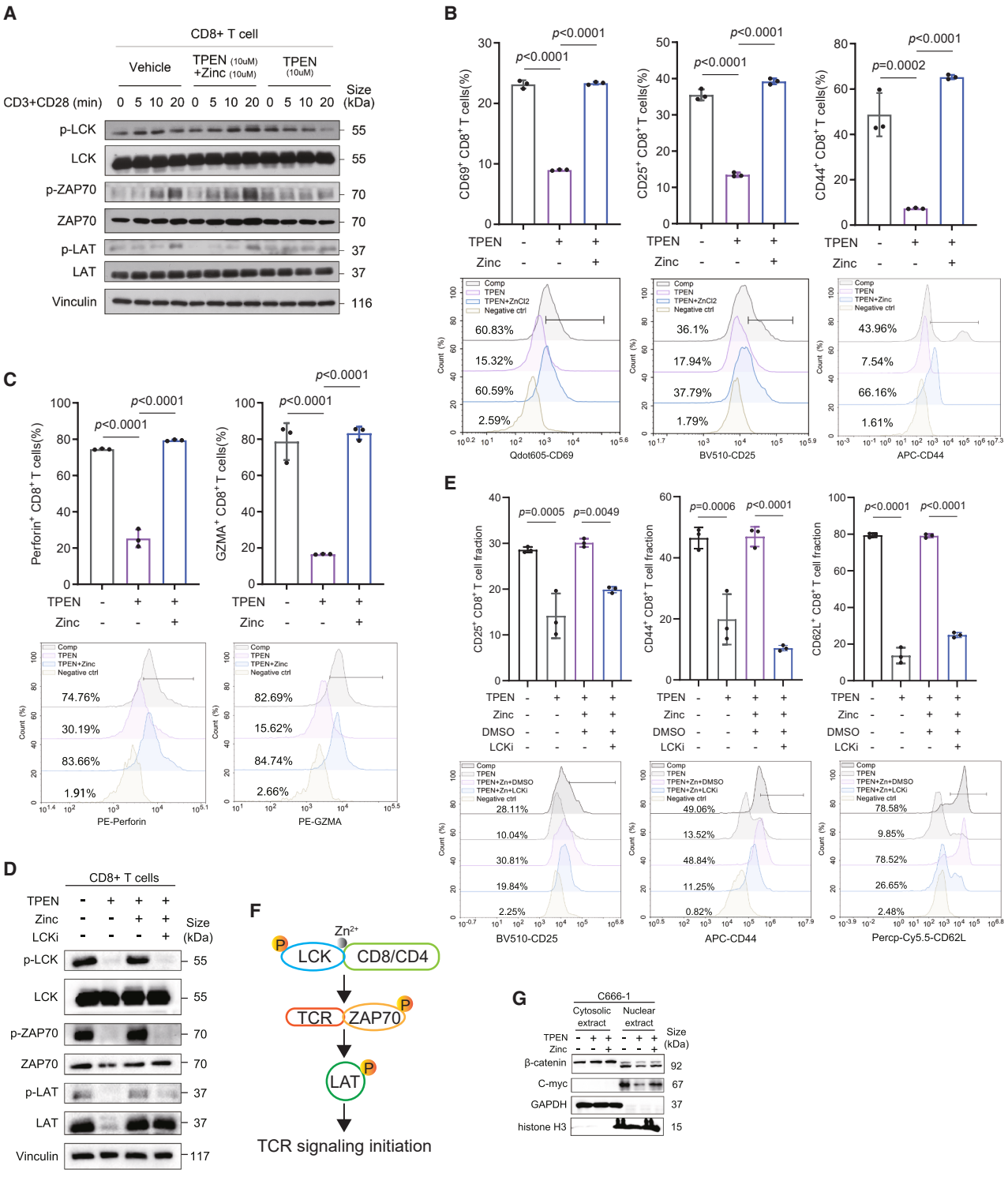

Figure 6. Zinc promotes LCK signaling phosphorylation in CD8⁺ T cells

(A) CD8⁺ T cells in medium lacking or supplying zinc and complete (vehicle) medium were stimulated for the indicated times (0, 5,10, and 20 min), and protein expression was analyzed by western blotting; phosphorylation sites include p-LCK(Y394), p-ZAP70(Y319), and p-LAT(Y171).

(B and C) Activated CD8⁺ T cells were cultured in a complete medium and medium neutralized with TPEN or re-added with zinc after neutralization for 24 h and analyzed for expression of the activation proteins (B) or cytotoxic granules (C) by flow cytometry (n = 3).

(D) Immunoblot analysis of CD8⁺ T cells activated in medium containing zinc and/or TPEN and/or LCK inhibitor (LCKi) for the indicated time periods.

(legend continued on next page)

the zinc concentration exceeded (50 μM) normal, no significant negative effects were observed on either tumor cells or $CD8^+$ T cells (Figures 5E and 5F). This suggested that excessive zinc intake by tumor cells might lead to zinc deficiency in $CD8^+$ T cells, thereby obstructing the TCR pathway and ultimately impairing their activation and proliferation (Figure S5E).

To validate the independent effects of ZIP14 on T cell function, we assessed ZIP14 levels in the parental cell lines (Figure S5F) and constructed ZIP14-KD C666-1 cells for subsequent experiments (Figure S5G). ZIP14-KD (Sh3 was selected) C666-1 with stable CD19 expression (S5H) was co-cultured with anti-CD19-CAR $CD8^+$ T cells. Zinc concentrations in both the medium and $CD8^+$ T cells were measured in this co-culture system. The results aligned with those reported by the SOX4 low-expressing group (Figures S5I and S5J), indicating that a reduction in ZIP14 or SOX4 expression in target cells led to a significant increase in zinc concentrations in both the surrounding environment and $CD8^+$ T cells (Figures 5G and 5H). Concomitantly, the reduction of ZIP14 in NPC cells effectively restored the activation of $CD8^+$ T cells (Figure S5K) and significantly augmented their cytotoxic effects (Figures S5L–S5P). To better elaborate the role of ZIP14 in the immunosuppressive internal environment, we used the CAR T system consistent with the SOX4 group for *in vivo* killing validation. The results demonstrated that NPC-specific ZIP14 KD prompted tumor shrinkage (Figure 5I) and the infiltration of activated and cytotoxic $CD8^+$ T cells (Figure 5J), which produced effects similar to those of SOX4.

Zinc homeostasis influences LCK signaling in CD8 T cells

The binding of CD8α to LCK during the activation of $CD8^+$ T cells is a zinc-dependent process.[59] We considered that removing zinc from the culture medium might significantly affect the stability and signal transduction of LCK. Therefore, we established zinc-deprived and zinc-restored groups to compare with the control group. Given that TCR signaling is typically activated rapidly within minutes, we extracted proteins from $CD8^+$ T cells at 5, 10, and 20 min post TCR activation. Subsequently, we analyzed the phosphorylation of key proteins involved in the TCR pathway. The results demonstrated that TCR pathway phosphorylation in the zinc reset group exhibited a trend similar to that of the control group, but zinc chelation effectively blocked the TCR activation (Figure 6A). Furthermore, we examined the expression of activation markers of $CD8^+$ T cells under these conditions, which suggested that zinc deficiency also profoundly impacted $CD8^+$ T cell activation (Figure 6B) and cytotoxicity (Figure 6C).

To further elucidate the role of zinc in LCK phosphorylation, we introduced an LCK inhibitor (LCKi). Immunoblotting (Figure 6D) and flow cytometry (Figure 6E) analysis demonstrated that supplementing zinc increased the number of activated, effector, and central memory-like $CD8^+$ T cells. Conversely, the addition of LCKi significantly reversed the zinc-promoted T cell activation. Notably, the addition of LCKi was comparable to TPEN in inhibiting $CD8^+$ T cell activation. In conclusion, zinc plays a pivotal role in the recruitment and phosphorylation of LCK (Figure 6F). Disruption of zinc homeostasis within the TME leads to the dephosphorylation of LCK, thereby blocking TCR signaling and impairing the cytotoxic capacity of $CD8^+$ T cells. Additionally, zinc deficiency can obstruct Wnt/β-catenin signaling in NPC (Figure 6G), the pathway identified as crucial for the development and progression of NPC, as discussed previously (Figures 2B, 2H, and 2I).

Targeting SOX4 is a safe and effective therapy against NPC

Our findings indicated that SOX4 is expressed explicitly in NPC cells and plays a dual role in promoting tumor formation, progression, and immune evasion, making it a promising target for therapeutic intervention. Nevertheless, pharmaceutical agents have yet to be specifically developed to target SOX4 up to today. Thus, we planned to use AAV to specifically inhibit SOX4 expression in subcutaneous NPC PDXs *in vivo*. AAV-mediated therapies have demonstrated low immunogenicity and low pathogenicity, proving to be a safe and effective method for delivering therapeutic genes to target cells in clinical trials for various diseases.[60] We employed an AAV-mediated SOX4 inhibition therapy to compare its effects against other first-line chemotherapy drugs, including gemcitabine (GEM) and cisplatin (DDP), in mice. The mouse PDX model was administered GEM, DDP, or AAV alone (Figure 7A). However, due to the occurrence of severe and irreversible dehydration and weight loss in over half of the mice in the DDP group, the experiment was terminated on day 12 following the initiation of treatment, by ethical guidelines. There was no significant difference in tumor size between the group treated with GEM alone and the control group. The DDP group exhibited the most pronounced inhibitory effect on tumor growth but also experienced the most severe adverse effects. In contrast, AAV-SOX4 RNAi administration not only remarkably suppressed tumor growth but also exhibited no adverse effects (Figures 7B and 7C).

Given extensive research on immunotherapy for NPC in recent years[61,62] and our experimental evidence on SOX4's regulatory role in NPC-infiltrating $CD8^+$ T cells, we postulated that combining SOX4-targeted AAV treatment with ICB could yield significant therapeutic benefits. Experiments were conducted using the PBMC-PDX humanized mouse model. Compared to anti-PD-1 monotherapy, AAV-SOX4-RNAi exhibited a modest advantage in tumor suppression, but the combination therapy demonstrated the most pronounced anti-tumor efficacy (Figures 7E and 7F). After the treatment, the tumor-infiltrating lymphocytes were subsequently analyzed by flow cytometry, showing a significant increase in the percentage of infiltrating effector $CD8^+$ T cells (Figure 7G) and cytotoxic $CD8^+$ T cells

(E) The effect of zinc, TPEN, and LCKi in $CD8^+$ T cell activation marker expression level change was analyzed through flow cytometry (n = 3).
(F) A schematic representation of the involvement of zinc in LCK signaling to activate the TCR pathway.
(G) Western blot of Wnt/β-catenin signaling in C666-1 cells under the different zinc conditions. (B, C, and E) The "n" value represents the number of biologically independent samples in each group. The data were presented as mean ± SD and analyzed using a one-way ANOVA test.

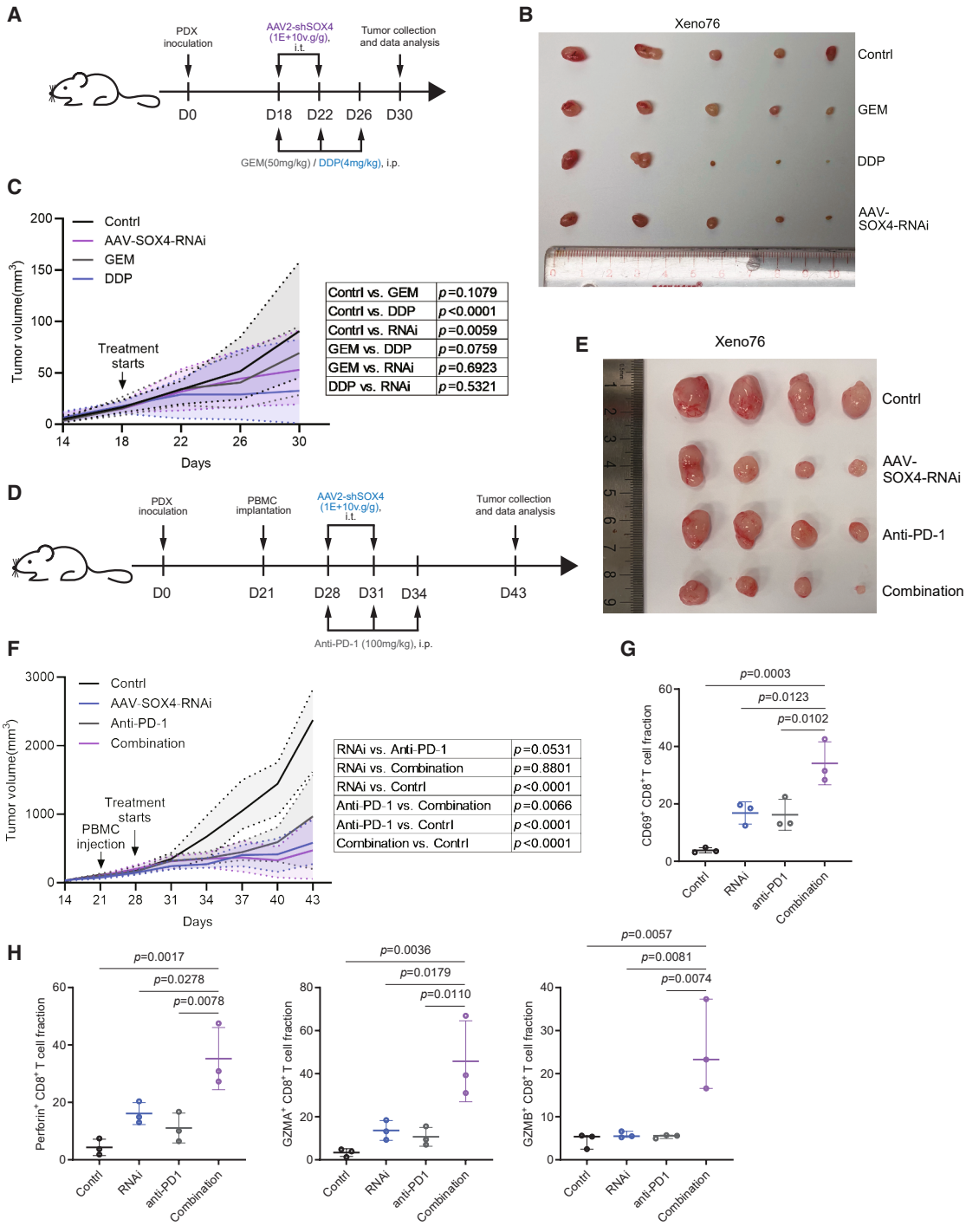

Figure 7. Estimation of SOX4-targeting therapeutic strategy in NPC treatment

(A) Schematic representation of the subcutaneous patient-derived xenograft (PDX) inoculation and chemotherapy strategy employed in nude mice.

(B) Tumors collected after a 12-day administration of various chemotherapies and AAV-SOX4-RNAi (n = 5).

(C) Tumor growth curves for GEM, DDP, and AAV-SOX4-RNAi treatments compared to the control group.

(D) A schematic illustrating the adoptive transfer of human PBMCs into NSG mice inoculated with PDX, along with the administration of monotherapy or combination therapy, which included anti-PD1 and/or AAV-SOX4-RNAi.

(E) PDX-derived tumors were collected at the experiment's endpoint.

(legend continued on next page)

(Figure 7H) under the combination therapy. Thus, the combination therapy was found to counteract the immunosuppressive and tumor-promoting effects of SOX4 via zinc metabolism, thereby reinvigorating anti-tumor immunity of $CD8^+$ T cells while simultaneously striking tumor cells.

DISCUSSION

Recent studies have begun investigating the role of metabolic remodeling within the TME concerning tumor immunosuppression. Given the limited efficacy of current immunotherapeutic regimens for patients with NPC and the lack of understanding of the unique immune microenvironment associated with NPC, an in-depth exploration of the role of tumor cells in reshaping the metabolic landscape of the TME, along with their dynamic interactions with immune cells, is essential for enhancing the effectiveness of immunotherapy. Zinc, a vital trace mineral element, functions as a crucial second messenger involved in fundamental cellular metabolic processes and plays significant physiological roles. As a key factor in maintaining cellular homeostasis, zinc has attracted increasing interest in the context of disease progression. Dysregulation in zinc metabolism often leads to dysfunctions in immune cells, particularly by disrupting signaling within the TCR pathway.

In our previous study, we established a multi-center cohort of patients with NPC that incorporated publicly available single-cell datasets. Through analyzing this cohort, we identified elevated expression of SOX4 in tumor cells as a master regulator of the cellular tumor phenotype. Furthermore, our findings demonstrate that tumor cells can activate competitive zinc uptake via the SOX4-ZIP14 pathway, reducing zinc levels within the TME, which may adversely affect T cell function. Zinc is essential for T cell activation and functionality, and zinc deficiency can lead to impaired T cell responses. Zinc exerts pleiotropic immunomodulatory effects across various immune cell populations. Although our study primarily investigates the role of ZIP14 in T cells, we acknowledge that dysregulation of zinc may concurrently influence multiple immune lineages through both direct cellular mechanisms and alterations within the TME. This complexity underscores the need for future research to systematically assess both the cell-type-specific and overall immunological consequences of modulating zinc transporter activity. Notably, our results indicated that T cells are more vulnerable to zinc deficiency than tumor cells—which often gain a competitive advantage for zinc within the TME. By manipulating zinc metabolism, tumor cells hinder T cell activation and function, depriving $CD8^+$ T cells of their cytotoxic capabilities and enabling tumor cells to evade immune surveillance. Therefore, inhibiting tumor-specific SOX4-ZIP14-zinc signaling is crucial for preserving the immune efficacy of tumor-infiltrating T cells.

In conclusion, our study concluded that SOX4, a frequently up-regulated MTF in NPC cells, not only promoted and sustained tumor-intrinsic properties but also manipulated microenvironmental zinc metabolism to outcompete T cells for zinc through the downstream target ZIP14. This interaction led to aberrant T cell TCR signaling, thereby impairing their anti-tumor immunity. A therapeutic strategy targeting SOX4 could rectify the abnormal zinc metabolism within the NPC TME and restore the cytotoxic function of tumor-infiltrating $CD8^+$ T cells by inhibiting the upstream regulator of the zinc transporter protein ZIP14, while also hindering the development and metastasis of tumor cells. This approach may represent a safe and effective method to enhance the efficacy of NPC immunotherapy combined with current induction chemotherapy.

Limitations of the study

This study provided evidence that SOX4 serves as a master regulator in the initiation, progression, and immune evasion of NPC by modulating zinc metabolism within the TME. However, the clinical application of targeting TFs remains challenging. We evaluated the efficacy of intratumoral delivery of AAV-SOX4-RNAi in a humanized mouse model, yet this approach is not widely implemented in clinical treatments. Furthermore, the absence of promising animal models for investigating the NPC immune microenvironment, particularly due to the lack of mouse-derived NPC cell lines and spontaneous mouse models, poses a significant challenge in studying NPC. Consequently, we were limited to utilizing PBMC-engrafted humanized models, which restricted our study window to approximately 6 weeks, to explore the NPC immune microenvironment.

RESOURCE AVAILABILITY

Lead contact

Further information and requests for resources and reagents should be directed to and will be fulfilled by the lead contact, Xin-Yuan Guan (xyguan@hku.hk).

Materials availability

Materials used in this study are available from the corresponding author upon request.

Data and code availability

- The single-cell sequencing data utilized in this study are publicly accessible in Gene Expression Omnibus (GEO) with the accession numbers GSE150825, GSE150430, and GSE162025. The bulk RNA sequencing data used are publicly available in GEO under accession numbers GSE102349, GSE53819, and GSE118719. The raw and processed Visium spatial sequencing data of primary NPC tissues have been deposited in GEO under accession number GSE200310. All accession numbers are listed in the key resources table.
- This study did not include any new or original code.
- Additional information needed in this article is available from the lead contact upon request.

ACKNOWLEDGMENTS

We would like to express our gratitude to the Imaging and Flow Cytometry Core of PanorOmic Sciences for their facility support and technical assistance.

(F–H) Tumor growth curves (F) were measured for the different groups (n = 4), and the proportions of tumor-infiltrating activated $CD8^+$ T cells (G) and cytotoxic $CD8^+$ T cells (H) were compared across each group (n = 3).
(C and F) The data were presented as mean ± SD and analyzed using a two-way ANOVA with Tukey's multiple comparisons test.
(G–H) The data were presented as mean ± SD and analyzed using a one-way ANOVA test.

This work was supported by grants including Theme-based Research Scheme Funds (TRS [T12-703/22-R], X.-Y.G.; TRS [T12-703/23-N], X.-Y.G.), Collaborative Research Funds (C7065-18GF, C7026-18GF, and C4039-19GF, X.-Y.G.), Research Impact Funds (R4017-18, R1020-18F, and R7022-20, X.-Y.G.), National Natural Science Foundation of China (81772554, X.-Y.G.; 82072738, X.-Y.G.; and 82103479, L.G.), Shenzhen Science and Technology Program (ZDSYS20210623091811035, X.-Y.G.; KQTD20180411185028798, X.-Y.G.; JCYJ20220818103014030, X.-Y.G.), and the Program for Guangdong Introducing Innovative and Entrepreneurial Teams (2019BT02Y198, X.-Y.G.). X.-Y.G. is the Sophie YM Chan Professor in Cancer Research at the University of Hong Kong.

AUTHOR CONTRIBUTIONS

Y.Y. designed the study and wrote the manuscript. S. Li, L.S., and J. Li collected the clinical samples. L.G., B.Z., and W.D. performed computational analysis. Y.Y. performed wet lab experiments with help from Q.L., J. Luo, Z.Q., X.F., J.H., B.L., S. Liu, H.Z., L.B., and C.N.W., and D.Z. and Y.Z. provided technical support. X.-Y.G. provided the wet lab space. X.-Y.G. and L.G. supervised the study, reviewed the manuscript, and provided grants. All authors have agreed with the manuscript for publication.

DECLARATION OF INTERESTS

The authors declare no competing interests.

STAR★METHODS

Detailed methods are provided in the online version of this paper and include the following:

- KEY RESOURCES TABLE
- EXPERIMENTAL MODEL AND STUDY PARTICIPANT DETAILS
  - Clinical samples
  - *In vivo* model
  - Establishment of the PBMC humanized mouse model and xeno-transplantation
  - Cell lines and culture
- METHOD DETAILS
  - Isolation of peripheral blood mononuclear cells from healthy donors
  - Anti-CD19 CAR lentivirus packaging and concentration
  - Transduction of $CD8^+$ T cells
  - Stable cell line construction
  - Cell viability and proliferation assays
  - Cell migration and invasion assays
  - Tumor sphere formation assay
  - Limiting dilution assay
  - CHIP-PCR
  - Dual luciferase reporter assay
  - Lactate dehydrogenase (LDH) release assay
  - Flow cytometry
  - Western blotting
  - Immunohistochemistry
  - RNA extraction and quantitative polymerase chain reaction (qPCR)
  - The enzyme-linked immunosorbent assay (ELISA)
  - Zinc assay
- QUANTIFICATION AND STATISTICAL ANALYSIS

SUPPLEMENTAL INFORMATION

Supplemental information can be found online at https://doi.org/10.1016/j.xcrm.2025.102300.

Received: January 2, 2025
Revised: June 3, 2025
Accepted: July 22, 2025
Published: August 15, 2025

REFERENCES

1. Bossi, P., Chan, A.T., Licitra, L., Trama, A., Orlandi, E., Hui, E.P., Halámková, J., Mattheis, S., Baujat, B., Hardillo, J., et al. (2021). Nasopharyngeal carcinoma: ESMO-EURACAN Clinical Practice Guidelines for diagnosis, treatment and follow-up. Ann. Oncol. *32*, 452–465.
2. Wei, X., Chen, B., Wang, Z., Zhao, P., and Duan, X. (2024). Nasopharyngeal cancer risk assessment by country or region worldwide from 1990 to 2019. BMC Public Health *24*, 1931.
3. Su, Z.Y., Siak, P.Y., Lwin, Y.Y., and Cheah, S.-C. (2024). Epidemiology of nasopharyngeal carcinoma: current insights and future outlook. Cancer Metastasis Rev. *43*, 919–939.
4. Liu, Z., Chen, Y., Su, Y., Hu, X., and Peng, X. (2021). Nasopharyngeal Carcinoma: Clinical Achievements and Considerations Among Treatment Options. Front. Oncol. *11*, 635737.
5. Lin, W., Chen, X., Huang, Z., Ding, Q., Yang, H., Li, Y., Lin, D., Lin, J., Zhang, H., Yang, X., et al. (2024). Identification of novel molecular subtypes to improve the classification framework of nasopharyngeal carcinoma. Br. J. Cancer *130*, 1176–1186.
6. Ma, Y., Zhou, H., Luo, F., Zhang, Y., Zhu, C., Li, W., Huang, Z., Zhao, J., Xue, J., Zhao, Y., et al. (2024). Remodeling the tumor-immune microenvironment by anti-CTLA4 blockade enhanced subsequent anti-PD-1 efficacy in advanced nasopharyngeal carcinoma. npj Precis. Oncol. *8*, 65.
7. Weidemüller, P., Kholmatov, M., Petsalaki, E., and Zaugg, J.B. (2021). Transcription factors: Bridge between cell signaling and gene regulation. Proteomics *21*, e2000034.
8. He, H., Yang, M., Li, S., Zhang, G., Ding, Z., Zhang, L., Shi, G., and Li, Y. (2023). Mechanisms and biotechnological applications of transcription factors. Synth. Syst. Biotechnol. *8*, 565–577.
9. Hu, H., Zhang, Q., Hu, F.-F., Liu, C.-J., and Guo, A.-Y. (2021). A comprehensive survey for human transcription factors on expression, regulation, interaction, phenotype and cancer survival. Brief. Bioinform. *22*, bbab002.
10. Reddy, J., Fonseca, M.A.S., Corona, R.I., Nameki, R., Segato Dezem, F., Klein, I.A., Chang, H., Chaves-Moreira, D., Afeyan, L.K., Malta, T.M., et al. (2021). Predicting master transcription factors from pan-cancer expression data. Sci. Adv. *7*, eabf6123. https://doi.org/10.1126/sciadv.abf6123.
11. Okita, Y., Kimura, M., Xie, R., Chen, C., Shen, L.T.W., Kojima, Y., Suzuki, H., Muratani, M., Saitoh, M., Semba, K., et al. (2017). The transcription factor MAFK induces EMT and malignant progression of triple-negative breast cancer cells through its target GPNMB. Sci. Signal. *10*, eaak9397.
12. Chaves-Moreira, D., Mitchell, M.A., Arruza, C., Rawat, P., Sidoli, S., Nameki, R., Reddy, J., Corona, R.I., Afeyan, L.K., Klein, I.A., et al. (2022). The transcription factor PAX8 promotes angiogenesis in ovarian cancer through interaction with SOX17. Sci. Signal. *15*, eabm2496. https://doi.org/10.1126/scisignal.abm2496.
13. Lukhele, S., Rabbo, D.A., Guo, M., Shen, J., Elsaesser, H.J., Quevedo, R., Carew, M., Gadalla, R., Snell, L.M., Mahesh, L., et al. (2022). The transcription factor IRF2 drives interferon-mediated CD8+ T cell exhaustion to restrict anti-tumor immunity. Immunity *55*, 2369–2385.
14. Fang, X.-L., Li, Q.J., Lin, J.Y., Huang, C.L., Huang, S.Y., Tan, X.R., He, S.W., Zhu, X.H., Li, J.Y., Gong, S., et al. (2024). Transcription factor ATMIN facilitates chemoresistance in nasopharyngeal carcinoma. Cell Death Dis. *15*, 112.
15. Yang, Z., Peng, Y., Wang, Y., Yang, P., Huang, Z., Quan, T., Xu, X., Sun, P., Sun, Y., Lv, J., et al. (2024). KLF5 regulates actin remodeling to enhance the metastasis of nasopharyngeal carcinoma. Oncogene *43*, 1779–1795.
16. Bagati, A., Kumar, S., Jiang, P., Pyrdol, J., Zou, A.E., Godicelj, A., Mathewson, N.D., Cartwright, A.N., Cejas, P., Brown, M., et al. (2021). Integrin αvβ6-TGFβ-SOX4 Pathway Drives Immune Evasion in Triple-Negative Breast Cancer. Cancer Cell *39*, 54–67.
17. Plaschka, M., Benboubker, V., Grimont, M., Berthet, J., Tonon, L., Lopez, J., Le-Bouar, M., Balme, B., Tondeur, G., de la Fouchardière, A., et al.

(2022). ZEB1 transcription factor promotes immune escape in melanoma. J. Immunother. Cancer *10*, e003484.

18. Ao, Y.Q., Gao, J., Jin, C., Wang, S., Zhang, L.C., Deng, J., Chen, Z.W., Wang, H.K., Jiang, J.H., and Ding, J.Y. (2023). ASCC3 promotes the immunosuppression and progression of non-small cell lung cancer by impairing the type I interferon response via CAND1-mediated ubiquitination inhibition of STAT3. Journal for immunotherapy of cancer *11*, e007766.
19. Sari, G., Dhatchinamoorthy, K., Orellano-Ariza, L., Ferreira, L.M., Brehm, M.A., and Rock, K. (2024). IRF2 loss is associated with reduced MHC I pathway transcripts in subsets of most human cancers and causes resistance to checkpoint immunotherapy in human and mouse melanomas. J. Exp. Clin. Cancer Res. *43*, 276.
20. Gong, L., Kwong, D.L.W., Dai, W., Wu, P., Li, S., Yan, Q., Zhang, Y., Zhang, B., Fang, X., Liu, L., et al. (2021). Comprehensive single-cell sequencing reveals the stromal dynamics and tumor-specific characteristics in the microenvironment of nasopharyngeal carcinoma. Nat. Commun. *12*, 1540.
21. Liu, Y., He, S., Wang, X.L., Peng, W., Chen, Q.Y., Chi, D.M., Chen, J.R., Han, B.W., Lin, G.W., Li, Y.Q., et al. (2021). Tumour heterogeneity and intercellular networks of nasopharyngeal carcinoma at single cell resolution. Nat. Commun. *12*, 741.
22. Chen, Y.-P., Yin, J.H., Li, W.F., Li, H.J., Chen, D.P., Zhang, C.J., Lv, J.W., Wang, Y.Q., Li, X.M., Li, J.Y., et al. (2020). Single-cell transcriptomics reveals regulators underlying immune cell diversity and immune subtypes associated with prognosis in nasopharyngeal carcinoma. Cell Res. *30*, 1024–1042.
23. Zhang, L., MacIsaac, K.D., Zhou, T., Huang, P.Y., Xin, C., Dobson, J.R., Yu, K., Chiang, D.Y., Fan, Y., Pelletier, M., et al. (2017). Genomic Analysis of Nasopharyngeal Carcinoma Reveals TME-Based Subtypes. Mol. Cancer Res. *15*, 1722–1732.
24. Lin, C., Zong, J., Lin, W., Wang, M., Xu, Y., Zhou, R., Lin, S., Guo, Q., Chen, H., Ye, Y., et al. (2018). EBV-miR-BART8-3p induces epithelial-mesenchymal transition and promotes metastasis of nasopharyngeal carcinoma cells through activating NF-κB and Erk1/2 pathways. J. Exp. Clin. Cancer Res. *37*, 283.
25. Bao, Y.N., Cao, X., Luo, D.H., Sun, R., Peng, L.X., Wang, L., Yan, Y.P., Zheng, L.S., Xie, P., Cao, Y., et al. (2014). Urokinase-type plasminogen activator receptor signaling is critical in nasopharyngeal carcinoma cell growth and metastasis. Cell Cycle *13*, 1958–1969.
26. Tiwari, N., Tiwari, V.K., Waldmeier, L., Balwierz, P.J., Arnold, P., Pachkov, M., Meyer-Schaller, N., Schübeler, D., van Nimwegen, E., and Christofori, G. (2013). Sox4 Is a Master Regulator of Epithelial-Mesenchymal Transition by Controlling Ezh2 Expression and Epigenetic Reprogramming. Cancer Cell *23*, 768–783.
27. Chen, X., Xu, M., Xu, X., Zeng, K., Liu, X., Pan, B., Li, C., Sun, L., Qin, J., Xu, T., et al. (2020). METTL14-mediated N6-methyladenosine modification of SOX4 mRNA inhibits tumor metastasis in colorectal cancer. Mol. Cancer *19*, 106.
28. Tan, X.Y., Li, Y.T., Li, H.H., Ma, L.X., Zeng, C.M., Zhang, T.T., Huang, T.X., Zhao, X.D., and Fu, L. (2023). WNT2-SOX4 positive feedback loop promotes chemoresistance and tumorigenesis by inducing stem-cell like properties in gastric cancer. Oncogene *42*, 3062–3074.
29. Wang, N., Liu, W., Zheng, Y., Wang, S., Yang, B., Li, M., Song, J., Zhang, F., Zhang, X., Wang, Q., and Wang, Z. (2018). CXCL1 derived from tumor-associated macrophages promotes breast cancer metastasis via activating NF-κB/SOX4 signaling. Cell Death Dis. *9*, 880.
30. Wang, J., Zhao, H., Xu, Z., and Cheng, X. (2020). Zinc dysregulation in cancers and its potential as a therapeutic target. Cancer Biol. Med. *17*, 612–625.
31. Grattan, B.J., and Freake, H.C. (2012). Zinc and cancer: implications for LIV-1 in breast cancer. Nutrients *4*, 648–675.
32. Wu, X., Wu, H., Liu, L., Qiang, G., and Zhu, J. (2020). Serum zinc level and tissue ZIP4 expression are related to the prognosis of patients with stages I–III colon cancer. Transl. Cancer Res. *9*, 5585–5594.
33. Li, M., Zhang, Y., Liu, Z., Bharadwaj, U., Wang, H., Wang, X., Zhang, S., Liuzzi, J.P., Chang, S.M., Cousins, R.J., et al. (2007). Aberrant expression of zinc transporter ZIP4 (SLC39A4) significantly contributes to human pancreatic cancer pathogenesis and progression. Proc. Natl. Acad. Sci. USA *104*, 18636–18641.
34. Bafaro, E., Liu, Y., Xu, Y., and Dempski, R.E. (2017). The emerging role of zinc transporters in cellular homeostasis and cancer. Sig Transduct Target Ther *2*, 17029.
35. Franklin, R.B., Feng, P., Milon, B., Desouki, M.M., Singh, K.K., Kajdacsy-Balla, A., Bagasra, O., and Costello, L.C. (2005). hZIP1 zinc uptake transporter down regulation and zinc depletion in prostate cancer. Mol. Cancer *4*, 32.
36. Zeng, Q., Liu, Y.M., Liu, J., Han, J., Guo, J.X., Lu, S., Huang, X.M., Yi, P., Lang, J.Y., Zhang, P., and Wang, C.T. (2019). Inhibition of ZIP4 reverses epithelial-to-mesenchymal transition and enhances the radiosensitivity in human nasopharyngeal carcinoma cells. Cell Death Dis. *10*, 588.
37. Tang, Y., Guo, S., Yu, N., and Li, H. (2024). ZIP4: a promising early diagnostic and therapeutic targets for pancreatic cancer. Am. J. Cancer Res. *14*, 4652–4664.
38. Zhang, P., Liu, R., and Lang, J. (2014). Zinc Transporter 4 (ZIP4): A Predictive Biomarker for Decreasing Radiosensitivity and Promoting Tumor Migration and Metastasis Through TGF-β–Dependent Manner in Nasopharyngeal Carcinoma (NPC). Int. J. Radiat. Oncol. Biol. Phys. *90*, S89–S90.
39. Hojyo, S., Miyai, T., Fujishiro, H., Kawamura, M., Yasuda, T., Hijikata, A., Bin, B.H., Irié, T., Tanaka, J., Atsumi, T., et al. (2014). Zinc transporter SLC39A10/ZIP10 controls humoral immunity by modulating B-cell receptor signal strength. Proc. Natl. Acad. Sci. USA *111*, 11786–11791.
40. Miyai, T., Hojyo, S., Ikawa, T., Kawamura, M., Irié, T., Ogura, H., Hijikata, A., Bin, B.H., Yasuda, T., Kitamura, H., et al. (2014). Zinc transporter SLC39A10/ZIP10 facilitates antiapoptotic signaling during early B-cell development. Proc. Natl. Acad. Sci. USA *111*, 11780–11785.
41. Liu, M.-J., Bao, S., Gálvez-Peralta, M., Pyle, C.J., Rudawsky, A.C., Pavlovicz, R.E., Killilea, D.W., Li, C., Nebert, D.W., Wewers, M.D., and Knoell, D. L. (2013). The zinc transporter SLC39A8 is a negative feedback regulator of NF-κB through zinc-mediated inhibition of IKK. Cell Rep. *3*, 386–400.
42. Yu, M., Lee, W.W., Tomar, D., Pryshchep, S., Czesnikiewicz-Guzik, M., Lamar, D.L., Li, G., Singh, K., Tian, L., Weyand, C.M., and Goronzy, J.J. (2011). Regulation of T cell receptor signaling by activation-induced zinc influx. J. Exp. Med. *208*, 775–785.
43. Gong, L., Yan, Q., Zhang, Y., Fang, X., Liu, B., and Guan, X. (2019). Cancer cell reprogramming: a promising therapy converting malignancy to benignity. Cancer Commun. *39*, 48.
44. Fang, X., Yan, Q., Liu, S., and Guan, X.-Y. (2022). Cancer Stem Cells in Hepatocellular Carcinoma: Intrinsic and Extrinsic Molecular Mechanisms in Stemness Regulation. Int. J. Mol. Sci. *23*, 12327.
45. Liu, B., Fang, X., Kwong, D.L.W., Zhang, Y., Verhoeft, K., Gong, L., Zhang, B., Chen, J., Yu, Q., Luo, J., et al. (2022). Targeting TROY-mediated P85a/AKT/TBX3 signaling attenuates tumor stemness and elevates treatment response in hepatocellular carcinoma. J. Exp. Clin. Cancer Res. *41*, 182.
46. Luo, J., Gong, L., Yang, Y., Zhang, Y., Liu, Q., Bai, L., Fang, X., Zhang, B., Huang, J., Liu, M., et al. (2024). Enhanced mitophagy driven by ADAR1-GLI1 editing supports the self-renewal of cancer stem cells in HCC. Hepatology *79*, 61–78.
47. Sureda-Gómez, M., Balsas, P., Rodríguez, M.L., Nadeu, F., De Bolòs, A., Eguileor, Á., Kulis, M., Castellano, G., López, C., Giné, E., et al. (2023). Tumorigenic role of Musashi-2 in aggressive mantle cell lymphoma. Leukemia *37*, 408–421.
48. Li, X., Zhao, Z., Zhang, X., Yang, S., Lin, X., Yang, X., Lin, X., Shi, J., Wang, S., Zhao, W., et al. (2017). Klf4 reduces stemness phenotype, triggers mesenchymal-epithelial transition (MET)-like molecular changes, and prevents tumor progression in nasopharygeal carcinoma. Oncotarget *8*, 93924–93941.

49. Chu, Q., Huang, H., Huang, T., Cao, L., Peng, L., Shi, S., Zheng, L., Xu, L., Zhang, S., Huang, J., et al. (2016). Extracellular serglycin upregulates the CD44 receptor in an autocrine manner to maintain self-renewal in nasopharyngeal carcinoma cells by reciprocally activating the MAPK/β-catenin axis. Cell Death Dis. *7*, e2456.

50. Yang, C.-F., Yang, G.D., Huang, T.J., Li, R., Chu, Q.Q., Xu, L., Wang, M.S., Cai, M.D., Zhong, L., Wei, H.J., et al. (2016). EB-virus latent membrane protein 1 potentiates the stemness of nasopharyngeal carcinoma via preferential activation of PI3K/AKT pathway by a positive feedback loop. Oncogene *35*, 3419–3431.

51. Luo, W., Gao, F., Li, S., and Liu, L. (2018). FoxM1 Promotes Cell Proliferation, Invasion, and Stem Cell Properties in Nasopharyngeal Carcinoma. Front. Oncol. *8*, 483.

52. Li, F., Song, X., Li, X., Zhang, X., Feng, X., Wang, L., Xu, L., Luo, J., Zhu, B., Ren, W., et al. (2020). Lgr5 maintains stemness and regulates cell property in nasopharyngeal carcinoma through Wnt/β-catenin signaling pathway. Stem Cell Res. *47*, 101916.

53. Qi, X.-K., Han, H.Q., Zhang, H.J., Xu, M., Li, L., Chen, L., Xiang, T., Feng, Q. S., Kang, T., Qian, C.N., et al. (2018). OVOL2 links stemness and metastasis via fine-tuning epithelial-mesenchymal transition in nasopharyngeal carcinoma. Theranostics *8*, 2202–2216.

54. Gong, L., Luo, J., Zhang, Y., Yang, Y., Li, S., Fang, X., Zhang, B., Huang, J., Chow, L.K.Y., Chung, D., et al. (2023). Nasopharyngeal carcinoma cells promote regulatory T cell development and suppressive activity via CD70-CD27 interaction. Nat. Commun. *14*, 1912.

55. Chen, P., Hsu, W.-H., Han, J., Xia, Y., and DePinho, R.A. (2021). Cancer Stemness Meets Immunity: From Mechanism to Therapy. Cell Rep. *34*, 108597.

56. Dianat-Moghadam, H., Mahari, A., Salahlou, R., Khalili, M., Azizi, M., and Sadeghzadeh, H. (2022). Immune evader cancer stem cells direct the perspective approaches to cancer immunotherapy. Stem Cell Res. Ther. *13*, 150.

57. Hushmandi, K., Einollahi, B., Saadat, S.H., Lee, E.H.C., Farani, M.R., Okina, E., Huh, Y.S., Nabavi, N., Salimimoghadam, S., and Kumar, A.P. (2024). Amino acid transporters within the solute carrier superfamily: Underappreciated proteins and novel opportunities for cancer therapy. Mol. Metab. *84*, 101952.

58. Chapman, N.M., Boothby, M.R., and Chi, H. (2020). Metabolic coordination of T cell quiescence and activation. Nat. Rev. Immunol. *20*, 55–70.

59. Lin, R.S., Rodriguez, C., Veillette, A., and Lodish, H.F. (1998). Zinc is essential for binding of p56(lck) to CD4 and CD8alpha. J. Biol. Chem. *273*, 32878–32882.

60. Naso, M.F., Tomkowicz, B., Perry, W.L., and Strohl, W.R. (2017). Adeno-Associated Virus (AAV) as a Vector for Gene Therapy. BioDrugs *31*, 317–334.

61. Gong, L., Kwong, D.L.W., Dai, W., Wu, P., Wang, Y., Lee, A.W.M., and Guan, X.Y. (2021). The Stromal and Immune Landscape of Nasopharyngeal Carcinoma and Its Implications for Precision Medicine Targeting the Tumor Microenvironment. Front. Oncol. *11*, 744889.

62. Wong, K.C.W., Hui, E.P., Lo, K.W., Lam, W.K.J., Johnson, D., Li, L., Tao, Q., Chan, K.C.A., To, K.F., King, A.D., et al. (2021). Nasopharyngeal carcinoma: an evolving paradigm. Nat. Rev. Clin. Oncol. *18*, 679–695.

STAR★METHODS

KEY RESOURCES TABLE

REAGENT or RESOURCE	SOURCE	IDENTIFIER
Antibodies		
Anti-beta Actin antibody [AC-15]	Abcam	ab6276; RRID:AB_2223210
Anti-CD8 alpha	Abcam	AB199016; RRID:AB_3699162
Anti-Fibronectin antibody (ab2413)	Abcam	ab2413; RRID:AB_2262874
Anti-Oct4 antibody [GT486]	Abcam	ab184665; RRID:AB_2895225
Recombinant Anti-KLF4 antibody [EPR19590]	Abcam	ab215036; RRID:AB_2933978
LAT Rabbit pAb	ABclonal	A5650; RRID:AB_2766410
LCK Rabbit pAb	ABclonal	A2177; RRID:AB_2764195
Phospho-LAT-Y171 Rabbit pAb	ABclonal	AP0809; RRID:AB_2771257
Phospho-LCK-Y394 Rabbit pAb	ABclonal	AP0182; RRID:AB_2771262
Phospho-ZAP70-Y319 Rabbit pAb	ABclonal	AP0467; RRID:AB_2771650
SOX4 Rabbit mAb	ABclonal	A21222; RRID:AB_3698515
ZAP70 Rabbit pAb	ABclonal	A2195; RRID:AB_2764212
InVivoMAb anti-human PD-1 (CD279)	Bio X Cell	BE0188; RRID:AB_10950318
Brilliant Violet 421™ anti-human/mouse Granzyme B Recombinant Antibody	BioLegend	396414; RRID:AB_2810603
Brilliant Violet 510™ anti-human CD25 Antibody	BioLegend	302639; RRID:AB_2629671
PE/Dazzle™ 594 anti-human Perforin Antibody	BioLegend	308132; RRID:AB_2687334
ZIP14 Rabbit pAb (A10413)	ABclonal	A10413; RRID:AB_2757961
Zombie NIR™ Fixable Viability Kit	BioLegend	423105
APC Mouse IgG1, kappa Isotype Ctrl	BioLegend	400119; RRID:AB_2888687
Brilliant Violet 605 anti-human CD69 Ab	BioLegend	310938; RRID:AB_2562307
Pacific Blue anti-human CD45 Antibody	BioLegend	304029; RRID:AB_2174123
E-Cadherin (24E10) Rabbit mAb	CST	3195s
GAPDH (14C10) Rabbit mAb	CST	2118
LAT (E3U6J) XP® Rabbit mAb	CST	45533S
N-cadherin	CST	4061
Phospho-Zap-70 (Tyr319)/Syk (Tyr352) (65E4) Rabbit mAb	CST	2717S
Snail (C15D3) Rabbit mAb	CST	3879S
Vimentin (5G3F10) Mouse mAb	CST	3390S
Amersham ECL Mouse IgG, HRP-linked whole Ab (from sheep)	Cytive	NA931-1ML
Amersham ECL Rabbit IgG, HRP-linked whole Ab (from donkey)	Cytive	NA934-1ML
ZIP14 Polyclonal Antibody	Invitrogen	PA5-87880; RRID:AB_2804476
Goat anti-Mouse IgG (H + L) Highly Cross-Adsorbed Secondary Antibody, Alexa Fluor 488	Invitrogen	A11029; RRID:AB_2534088
Goat anti-Rabbit IgG (H + L) Cross-Adsorbed Secondary Antibody, Alexa Fluor 555	Invitrogen	A-21428; RRID:AB_2535849
c-Myc Monoclonal Antibody (9E10)	LifeTech	132500; RRID:AB_2533008
beta Catenin (CTNNB1) Mouse Monoclonal Antibody	Origene	UM500015; RRID:AB_2629030
Monoclonal Anti-Vinculin antibody produced in mouse	Sigma-Aldrich	V9131; RRID:AB_477629

(*Continued on next page*)

Continued

REAGENT or RESOURCE	SOURCE	IDENTIFIER
Chemicals, peptides, and recombinant proteins		
Zinc chloride, 50 G	Sigma-Aldrich	Z0152-50G
Lck Inhibitor	MCE	HY-12072
Lipofectamine™ 3000 Transfection Reagent	Thermo Fisher	L3000075
TRIzol RNA Isolation Reagents	Thermo Fisher	15596026
Premix Ex TaqTM (Probe qPCR)	TAKARA	RR390W
T4 DNA Ligase	TAKARA	2011B
Puromycin	Sigma-Aldrich	P9620
dimethyl sulfoxide	Sigma-Aldrich	D2650
Polybrene	Sigma-Aldrich	TR-1003
Formaldehyde solution 4%	Sigma-Aldrich	1.00496
Triton X-100	Sigma-Aldrich	X100-500ML
BSA	Sigma-Aldrich	A3059-100G
FastStartTm Tag DNA Polymerase	ROCHE	04738403001
N,N,N,N′-Tetrakis(2-pyridylmethyl) ethylenediamine, 50 MG	Sigma-Aldrich	P4413-50MG
TexMACS GMP Medium	Miltenyi Biotec	170-076-306
T cell TransAct™, human	Miltenyi Biotec	130-128-758
Human IL-2 IS, premium grade, 50 μg	Miltenyi Biotec	130-097-745
human recombinant EGF	Life Technologies	PHG0315
human recombinant FGF	Life Technologies	PHG0261
Penicillin/Streptomycin	Invitrogen	15070063
FastDigest EcoRI	Invitrogen	FD0274
FastDigest BamHI	Invitrogen	FD0054
B27	Invitrogen	17504044
RIPA buffer	Invitrogen	89900
DAPI	Invitrogen	D1306
Trypsin-EDTA	Gibco	25200072
Fetal Bovine Serum	Gibco	16000036
Target Retrieval Solution	DAKO	S1699
Liquid DAB+ Substrate Chromogen System	DAKO	K3468
2x Laemmli Sample Buffer	Bio-Rad	1610737
Clarityrm Western ECL Substrate	Bio-Rad	170–5061
insulin	Biological Industries	41-975-100
Critical commercial assays		
ClonExpress II One Step Cloning Kit	Vazyme	C112-01
Immunoprecipitation Kit (Protein G)	ROCHE	11719386001
CellTiter 96® AOueous Non-RadioactiveCell Proliferation Assay (MTS)	Promega	G5421
LDH-Glo™ Cytotoxicity Assay	Promega	J2381
IFN gamma Human ELISA Kit	Invitrogen	KHC4022
TNF alpha Human ELISA Kit	Invitrogen	KHC3011
Bio-Rad Protein Assay Kit I	Bio-Rad	5000001
EZ-ChIP kit	Merck	17–371
FITC Annexin V Apoptosis Detection Kit I	BD PharmingenTM	556547
PE Annexin V Apoptosis Detection Kit I	BD PharmingenTM	559763
Zinc Assay Kit (Cell-based)	Abcam	ab241014
Zinc Assay Kit	Abcam	ab102507

(*Continued on next page*)

Continued

REAGENT or RESOURCE	SOURCE	IDENTIFIER
Deposited data		
Single cell RNA-Seq	Gene Expression Omnibus	GSE150825
Single cell RNA-Seq	Gene Expression Omnibus	GSE150430
Single cell RNA-Seq	Gene Expression Omnibus	GSE162025
RNA-Seq	Gene Expression Omnibus	GSE118719
RNA-Seq	Gene Expression Omnibus	GSE102349
RNA-Seq	Gene Expression Omnibus	GSE53819
Spatial transcriptomics	Gene Expression Omnibus	GSE200310
Experimental models: Cell lines		
C666-1	The NPC Tissue Bank, HKU	N/A
NPC43-EBV+	The NPC Tissue Bank,HKU	N/A
NPC43-EBV-	The NPC Tissue Bank,HKU	N/A
NP69	The NPC Tissue Bank,HKU	N/A
NP460	The NPC Tissue Bank,HKU	N/A
HEK293FT	Thermo Fisher Scientific	R70007
Experimental models: Organisms/strains		
BALB/c nude mice	Center for Comparative Medicine Research, HKU	N/A
NOD-SCID	Center for Comparative Medicine Research, HKU	N/A
NSG	Center for Comparative Medicine Research, HKU	N/A
One Shot™ Stbl3™ Chemically Competent E. coli	Invitrogen	C737303
Oligonucleotides		
ShNC-F: CCGGCCTAAGGTTAAGTCGCCCTCGCT CGAGCGAGGGCGACTTAACCTTAGGTTTTTG	GENEWIZ	N/A
ShNC-R: AATTCAAAAACCTAAGGTTAAGTCGCCC TCGCTCGAGCGAGGGCGACTTAACCTTAGG	GENEWIZ	N/A
SOX4-Sh2-F: CCGGAGCGACAAGATCCCTTTCATT CTCGAGAATGAAAGGGATCTTGTCGCTTTTTG	GENEWIZ	N/A
SOX4-Sh2-R: AATTCAAAAAAGCGACAAGATCCCTT TCATTCTCGAGAATGAAAGGGATCTTGTCGCT	GENEWIZ	N/A
SOX4-Sh3-F: CCGGTGGGCACATCAAGCGACCCA TCTCGAGATGGGTCGCTTGATGTGCCCATTTTTG	GENEWIZ	N/A
SOX4-Sh3-R: AATTCAAAAATGGGCACATCAAGCGA CCCATCTCGAGATGGGTCGCTTGATGTGCCCA	GENEWIZ	N/A
SLC39A14-Sh2-F: CCGGTCAACCCTCTGGAAGATT ATTCTCGAGAATAATCTTCCAGAGGGTTGATTTTTG	GENEWIZ	N/A
SLC39A14-Sh2-R: AATTCAAAAATCAACCCTCTGGA AGATTATTCTCGAGAATAATCTTCCAGAGGGTTGA	GENEWIZ	N/A
SLC39A14-Sh3-F: CCGGGAGCGACGGCCTCCATAA TTTCTCGAGAAATTATGGAGGCCGTCGCTCTTTTTG	GENEWIZ	N/A
SLC39A14-Sh2-R: AATTCAAAAAGAGCGACGGCCT CCATAATTTCTCGAGAAATTATGGAGGCCGTCGCTC	GENEWIZ	N/A
GAPDH-F: AGCCACATCGCTCAGACAC	GENEWIZ	N/A
GAPDH-R: GCCCAATACGACCAAATCC	GENEWIZ	N/A
β-actin-F: CCAGCTGCTTCCATACCCAA	GENEWIZ	N/A
β-actin-R: TGCCAGTTCCAGTTCCCTAG	GENEWIZ	N/A
18S-F: GTAACCCGTTGAACCCCATT	GENEWIZ	N/A
18S-R: CCATCCAATCGGTAGTAGCG	GENEWIZ	N/A
SLC39A14-F: TGGACACAGCCATTATGCCTC	GENEWIZ	N/A

(*Continued on next page*)

Continued

REAGENT or RESOURCE	SOURCE	IDENTIFIER
SLC39A14-R: GAGTAGCGGACACCTTTCAGC	GENEWIZ	N/A
SOX4-F: AGCGACAAGATCCCTTTCATTC	GENEWIZ	N/A
SOX4-R: CGTTGCCGGACTTCACCTT	GENEWIZ	N/A
CHIP-PCR-No.1-F: AGCCACATCGCTCAGACAC	GENEWIZ	N/A
CHIP-PCR-No.1-R: GCCCAATACGACCAAATCC	GENEWIZ	N/A
CHIP-PCR-No.2-F: CCAGCTGCTTCCATACCCAA	GENEWIZ	N/A
CHIP-PCR-No.2-R: TGCCAGTTCCAGTTCCCTAG	GENEWIZ	N/A
CHIP-PCR-No.3-F: GTAACCCGTTGAACCCCATT	GENEWIZ	N/A
CHIP-PCR-No.3-R: CCATCCAATCGGTAGTAGCG	GENEWIZ	N/A
Recombinant DNA		
PLKO.1-PURO	Sigma-Aldrich	SHC001
Software and algorithms		
Extreme Limiting Dilution Analysis (ELDA)	WEHI Bioinformatics	ELDA: Limiting Dilution Analysis for stem cell research
NovoExpress software	Agilent	v 1.5.6
GraphPad Prism 10	GraphPad	v 10.1.2
SPSS Statistics	IBM	22.0
ImageJ	ImageJ	https://doi.org/10.1038/nmeth.2089

EXPERIMENTAL MODEL AND STUDY PARTICIPANT DETAILS

Clinical samples

This study was conducted with the approval of the ethics committee from the University of Hong Kong, the University of Hong Kong-Shen Zhen Hospital, and the Hong Kong Red Cross. All the research was under the guidance of associated ethical regulations. Clinical samples for sequencing, primary culture, immunostaining, and flow cytometry analysis were obtained from healthy blood donors and patients with NPC and lymphatic hyperplasia, who have signed informed consent.

In vivo model

All animal procedures and work were performed in strict adherence to the Animals (Control of Experiments) Ordinance (Hong Kong) and the Institute's guidelines from the Center for Comparative Medical Research (CCMR), Li Ka Shing Faculty of Medicine, The University of Hong Kong. For the tumorigenicity model, 1.5×10^6 human shSOX4 C666-1 cells, 3×10^6 human SOX4-OE NP69 cells, and their corresponding control groups were injected subcutaneously into 4∼6-week BALB/c nude mice using 100 μL of sterile PBS. Tumor volumes were measured with a digital caliper using the long (L) and width (W) diameters and calculated using the formula $V=(L\times W^2)/2$. To establish the lung metastatic model, female NOD SCID mice aged 4–6 weeks were injected with 2×10^6 human shNC/shSOX4 C666-1 cells intravenously and left for 8 weeks. After the experiment, imaging of live mice and removed lungs were taken, and the lungs were dissected for histological examination.

Establishment of the PBMC humanized mouse model and xenotransplantation

Freshly isolated PBMCs were stimulated with T cell TransAct, human (Miltenyi) for three days and expanded in TexMACS GMP medium (Miltenyi) with the addition of 10% Hi-FBS and 1% PS, 50 IU/mL IL-2 (Miltenyi) for another three days. 6-week-old female NSG mouse had received an intravenous injection of 1×10^7 activated PBMCs in 160 μL PBS. On day 7 after PBMCs injection, 3×10^6 SOX4-NC/KD C666-1 cells were injected subcutaneously on the left dorsal flank of each mouse. The human immune function began regenerating one week after PBMC injection and was assessed on day 14 by labeling mouse PBMCs with FITC anti-human CD45 antibody. The tumors were collected for flow cytometry analysis on day 21.

For the xenotransplanted humanized mouse model, 4-week-old female NSG mice were maintained under anesthesia by intraperitoneal injection of ketamine (10mg/kg body weight) and xylazine (5mg/kg body weight) mixture. Xeno76 kept on nude mice was minced by a scalpel blade into tiny pieces with an identical volume (2 mm × 2 mm × 2 mm). Pieced PDX tissue was inoculated subcutaneously into the left dorsal flank of each mouse via a puncture needle. After 3 weeks when the PDX started to grow, 1×10^7 activated PBMCs in 160 μL PBS were injected intravenously into the xenotransplanted NSG mice. Day 7 post-PBMC injection, the tumor-bearing mice were divided into four groups randomly and administrated with AAV-shNC, AAV- shSOX4, anti-PD1, and combination therapy for a week, the tumors were collected for flow cytometry analysis. AAVs (AAV-shNC or AAV-shSOX4) produced by Genechem Co., Ltd (Shanghai, China) were intratumorally injected twice at 3-day intervals with 2×10^{11} vg/mouse (on day 28 and

31). Intraperitoneal injection of an anti-PD-1 antibody (Clone J116; Bio-XCell, West Lebanon, NH, USA) on days 28, 31 and 34. Tumor volumes were measured with a digital caliper using the long (L) and width (W) diameters and calculated using the formula $V=(L\times W^2)/2$.

Cell lines and culture

All cell lines in this study maintained at 37°C in humidified incubators containing 5% CO2. Human NPC cell lines C666-1 (EBV+), NPC43 (EBV+ and EBV−), and human NPE cell lines NP460, NP69 were provided by The NPC Tissue Bank, the University of Hong Kong. The HEK293FT cell line was purchased from Thermo Fisher Scientific and cultured according to recommendations. All NPC and NPE cell lines were cultured in RPMI-1640 (Gibco) supplemented with 10% FBS (Gibco) and 1% PS (Gibco). The HEK293FT cell line was cultured in DMEM (Gibco) supplemented with 10% FBS (Gibco), 1% PS (Gibco), 1× MEM amino acids solution (Gibco) and 1 mM sodium pyruvate (Gibco). Cell lines have been tested for authenticity by performing STR profiling and were free of mycoplasma before use.

METHOD DETAILS

Isolation of peripheral blood mononuclear cells from healthy donors

The peripheral blood from healthy donors was collected by Hong Kong Red Cross and approved for medical research. All donors gave formal consent for their blood to be used in this study. The collected citrate phosphate dextrose (CPD) anticoagulated peripheral blood was mixed with phosphate-buffered saline (PBS) containing 0.5% EDTA at a 1:1 ratio. 10 mL Ficoll-Paque PLUS (Cytiva) transferred into 50 mL conical tube then gently covering 35 mL blood mixture. The blood mixture was centrifuged at 400×g with the lowest acceleration and deceleration speed for 25 mins at room temperature. The PBMCs at the second layer were collected into new 50 mL conical tubes and centrifuged at 300×g for 10 mins. The supernatant was discarded. PBMCs were washed with PBS containing 2% FBS (Gibco) and 0.5% EDTA once, centrifuged, and discarded supernatant. ACK Lysing Buffer (Gibco) was used for red blood cell lysing according to the manufacturer's description. The fresh PBMCs were ready for T cell isolation and activation. For PBMCs frozen, 90% FBS supplemented by 10% DMSO (Sigma) was prepared as the freezing medium. PBMCs cryopreserved in Corning CoolCell LX at −80°C overnight then transferred into liquid nitrogen for long-term storage. PBMCs isolated for less than one month were used in this study.

Anti-CD19 CAR lentivirus packaging and concentration

HEK293FT cells were seeded at the confluency of 95% per well in a six-well plate using DMEM transfection medium. Cells were transfected with the packaging plasmids psPAX2 (Addgene) and pMD2.G (Addgene) together with the CAR overexpression plasmid (pLV[Exp]-EGFP-EF1A-CD19-CAR) in a 2:1:4 ratio, utilizing the Lipofectamine 3000 transfection reagent (Invitrogen) by the instructions provided by the manufacturer. The lipid-DNA complex was incubated for 6 hours. Replaced medium completely with a fresh lentivirus packaging medium supplemented with 1× viral boost reagent (Alstem), following the instructions of the manufacturer.

Lentivirus was collected at 24-, 48- and 72-h post-transfection. Cell medium containing the lentivirus was centrifuged at 1,000×g, 4°C for 15 min to remove the cell debris. We concentrated on the lentivirus particles by mixing them with Lenti-X Concentrator (TaKaRa), according to the manufacturer's protocols. The mixture was incubated at 4°C for 30 min before being centrifuged at 1500×g for 45 min at 4°C. The lentivirus pellet was subsequently resuspended in cold PBS to create the 100× concentrated virus.

Transduction of $CD8^+$ T cells

Human $CD8^+$ T cells were isolated from human PBMCs were activated with T cell TransACT (Miltenyi) per the manufacturer's protocol for 12 h. Activated human $CD8^+$ T cells with a cell density of 2×10^6/mL were mixed with the concentrated lentivirus (50 μL/mL) cultured into each well of 24-well plates and supplemented with 10 μg/mL Protamine Sulfate, 200 IU/mL hIL2 and T cell TransACT (Miltenyi). The mixture was then centrifuged at 1,000× g at 32°C for 90 min followed by incubation for 24 h 1 mL of complete T cell culture medium supplemented with 25 IU/mL hIL-2 was added to each well and incubated for 24 h. $CD8^+$ T cells expressing Anti-CD19-CAR were sorted based on strong EGFP expression by using BD FACS Aria SORP.

Stable cell line construction

The lentiviruses of overexpressing of SOX4 (LV-SOX4) and control (LV-CON) from Genechem Co., Ltd. (Shanghai, China). Stable cell lines were generated by selecting transfected cells with Puromycin (3 μg/mL, Gibco, NY). For knockdown, plasmids expressing short hairpin RNAs (shRNA) targeting human SOX4 and ZIP14 were built by cloning shRNA sequences into the lentiviral vector pLKO.1 (Sigma, SHC001). ShNC is a negative control containing a sequence that does not target any known mammalian genes. These stable knockdown cell lines were selected by puromycin dihydrochloride (3 μg/mL, Gibco, NY).

Cell viability and proliferation assays

Lentiviral transduced cell lines were seeded into 96-well plates (Corning) with a density of 1×10^3/well in 100 μL of medium. Cell Titer-Glo luminescent reagent (Promega) was added each day from Day 1 to Day 6 and plates were read using a microplate reader after 2 h of incubation in the dark following the manufacturer's description. Foci formation assay was performed as previously described. Cells

were seeded at 1×10^3 cells per well in 6-well plates and incubated for two weeks until visible colonies formed. Cells were fixed by 3.7% formaldehyde in PBS and stained with crystal violet. Colonies were counted by ImageJ.

Cell migration and invasion assays

Lentiviral transduced C666-1 (NC and SOX4 KD) and NP69 cells (Vector, SOX4 OE) were assayed for their abilities to spread and invade through wound-healing, Boyden chamber and invasion assays as described previously1. 2×10^5 cells (NP69) or 1×10^5 cells (C666-1) were seeded into the inner chamber in serum-free medium, and cells were challenged with 10% FBS-containing medium in the outer chamber. Matrigel coated invasion inserts (Corning) with 8 μm pore membranes were used for invasion assays. Cells were incubated at 37°C in 5% CO_2 for 24h. Cotton swabs were used to remove the cells on the inside of transwell insert, and cells onto the bottom of the insert were fixed in 4% formaldehyde (Sigma-Aldrich) and stained with crystal violet. The number of cells in three random fields of pictures were tallied to determine the average number of cells per field that had transmigrated.

Tumor sphere formation assay

The culture medium constituted by DMEM/F12 medium (Gibco) supplemented with 2% B27 (Life Technologies), 4 μg/mL insulin (Invitrogen), 20 ng/mL human recombinant EGF (Sigma-Aldrich), 10 ng/mL basic FGF (Millipore) and 1% methylcellulose (Sigma-Aldrich). The constructed cell lines were seeded at 1×10^4 or 2×10^4 cells were cultured into 6-well ultra-Low Attachment plates (Costar) and replenished with 500 μL of the supplemented medium every two days. Spheres were counted after one week of culture.

Limiting dilution assay

Lentiviral transduced NP69 cells (SOX4-OE and vector) underwent serial dilution to obtain suitable concentrations for subcutaneous injection into 4∼6-week-old female NOD SCID mice. The count of mice that developed tumors within two months post-transplantation was counted from each group, and images of tumors formed were taken. The frequency of estimated stem cells and the significance of the difference between treatment groups were evaluated using the Extreme Limiting Dilution Analysis (ELDA) software.

CHIP-PCR

SOX4-3×FLAG construct incorporated into the CV702 vector (purchased from Shanghai Genechem Co., Ltd.). EZ-ChIP kit (Merck) was used for this experiment. Briefly, C666-1 cells were cross-linked with formaldehyde for 10 min at room temperature, followed by quenching with glycine. Chromatin was then sonicated to generate 200–500 bp fragments using Bioruptor Pico. Immunoprecipitation was carried out overnight at 4°C with with Anti-FLAG M2 Antibody (CST, #2368) coupled to Protein A/G Magnetic Beads (Pierce). After stringent washing, DNA-protein complexes were eluted and reversed cross-linking. Purified DNA was analyzed by PCR with primers flanking the putative binding sites in the SOX4 promoter.

Dual luciferase reporter assay

HEK293FT cells were seeded at 80–90% confluency into 96-well plates and transfected using Lipofectamine 3000 (Life Technologies) as per the manufacturer's manuals. In brief, 100 ng of Renilla phRL-TK control plasmid along with 100 ng of each experimental plasmid (CV702-NC, CV702-SOX4) were transfected in the presence of GV238-SLC39A14-firefly_luciferase plasmid. The Dual-Glo Luciferase Assay System (Promega) was utilized to measure the Relative luciferase units (RLUs) 48 h after transfection. The RLUs from firefly luciferase signal were normalized by the Renilla signal.

Lactate dehydrogenase (LDH) release assay

The LDH activity was evaluated employing the LDH-Glo Cytotoxicity Assay, in accordance with the instructions provided by the manufacturer (Promega). In summary, following a 24-h co-culture, 2 μL of conditioned medium (CM) was extracted from each sample and diluted in 48 μL of LDH storage buffer. Subsequently, the prepared LDH detection reagent was added at a 1:1 ratio and incubated at room temperature for 60 min. The fluorescence intensity was then measured using a CLARIOstar Plus microplate reader (BMG Labtech).

Flow cytometry

For surface marker analysis, the cells were collected, and the supernatant was discarded. The cells were then washed once with FACS buffer (1× PBS containing 0.5% EDTA and 2% FBS), followed by centrifugation at 300×g for 5 min at each step. The cells resuspended in FACS buffer and incubated with the appropriate surface marker antibodies for 20 min at 4°C. After incubation, the cells were washed with 2 mL of FACS buffer, centrifuged at 300×g for 5 min, and the supernatant was discarded. The cells were then resuspended in FACS buffer for further analysis. For intracellular marker analysis, the cells were fixed and permeabilized using BD Cytofix/Cytoperm, according to the manufacturer's instructions. The stained cells were subsequently washed and resuspended in 1× Perm buffer for flow cytometry analysis. The intensity of the conjugated fluorochromes was detected using a NovoCyte Quanteon flow cytometer (Agilent), with analysis performed using NovoExpress software (v 1.5.6, Agilent). Gating strategies were presented in supplement Figure S6.

Western blotting

Cells were lysed in Pierce RIPA Buffer (Thermo Fisher Scientific), supplemented with Protease Inhibitor Cocktail (MCE) and Phosphatase Inhibitor Cocktail (MCE). Cytoplasmic and nuclear proteins were extracted using the Cytoplasmic & Nuclear Protein Extraction Kit (Beyotime). Protein lysates were quantified via the Bradford protein assay, separated by SDS-PAGE, and transferred to an activated PVDF membrane (Millipore). After blocking, the membrane was incubated with the primary antibody overnight at 4°C, followed by incubation with an HRP-conjugated secondary antibody in TBST buffer for 1 h at room temperature. Each antibody incubation was followed by three washes with 1×TBST (100 rpm, 10 min, three times). Blots were visualized using enhanced chemiluminescence (Bio-Rad) and X-ray film. Band intensities were normalized to β-Actin, vinculin, or GAPDH.

Immunohistochemistry

For immunohistochemistry (IHC) staining, we collected formalin-fixed paraffin-embedded (FFPE) NPC sections from the Department of Pathology at the University of Hong Kong-Shenzhen Hospital. IHC was performed following standard protocols. Briefly, the tissue slides were placed in a 65°C oven for a minimum of 3 h and then sequentially immersed in xylene (three times), a 1:1 mixture of xylene and ethanol, 100% ethanol, 95% ethanol, and 75% ethanol, with each step lasting 10 min. The slides were then rinsed with tap water to ensure complete dewaxing. Next, the slides were immersed in 1× antigen retrieval buffer (Dako) for 45 min at 95°C and allowed to cool naturally for at least 30 min. The slides were washed three times with phosphate-buffered saline (PBS) and incubated with 3% hydrogen peroxide (H_2O_2) for 10 min at room temperature. Following additional washes with PBS, the slides were incubated with a blocking buffer for 1 h at room temperature. The slides were then incubated overnight at 4°C with anti-human SOX4 antibody (Abcam, 1:100) and anti-human GZMA (Abcam, 1:100) in PBS containing 1% bovine serum albumin (BSA). The following day, the slides were washed three times with PBS for 5 min each and treated with labeled polymer-HRP and DAB substrate using the Real EnVision Detection Systems Peroxidase/DAB, Rabbit/Mouse (Dako), according to the manufacturer's instructions. Subsequently, the slides were washed, stained with hematoxylin (Thermo Fisher), and dehydrated in the reverse order of hydration. Finally, the slides were mounted with DPX mounting medium (Sigma), and images were captured using a color imaging microscope.

For immunofluorescence (IF) staining, the slides were blocked with 3% BSA in PBS for 1 h at room temperature and subsequently incubated with primary antibodies, including anti-human SOX4 (Abcam) and anti-human SLC39A14 (Abclonal), at 4°C overnight. Following three washes with PBS, the slides were incubated with Alexa 488 goat anti-mouse (Invitrogen) and Alexa 555 goat anti-rabbit (Invitrogen) antibodies for 1 h at room temperature. After another set of three washes with PBS, the slides were treated with DAPI at a concentration of 1:1000 for 10 min at room temperature. The slides were then sealed with Diamond antifade mountant (Invitrogen), and images were captured using the LSM900 Microscope System.

RNA extraction and quantitative polymerase chain reaction (qPCR)

Total RNA was extracted using the RNA Extraction Kit from Vazyme. Complementary DNA was synthesized from 2 μg of total RNA utilizing the PrimeScript RT Reagent Kit with the gDNA eraser from Takara. Quantitative real-time PCR (qRT-PCR) was conducted with TB Green Premix Ex Taq from TaKaRa and analyzed using the LightCycler 480 II Real-Time PCR Detector from Roche. The quality of the amplified fragments was evaluated through the melting curve method. Transcript levels were normalized to ACTB and the relative mRNA levels in experimental samples were compared to controls.

The enzyme-linked immunosorbent assay (ELISA)

Cell culture medium from the co-culture system was collected after 24 h of incubation. Enzyme-linked immunosorbent assay (ELISA) was employed to quantify the secretion of cytokines, including tumor necrosis factor-alpha (TNF-α) (Invitrogen), and interferon-gamma (IFN-γ) (Abcam). The concentrations of these cytokines in the cell culture supernatants from various experimental groups were measured at wavelengths of 450 nm and 620 nm, and the results were calculated using their respective standard curves.

Zinc assay

Intracellular and extracellular zinc quantification procedures were conducted following the manufacturer's instructions. For the quantification of medium zinc (ab102507), a 7% TCA solution was added to the collected samples at a 1:1 ratio for deproteinization. The mixture was then centrifuged at maximum speed for 5 min. Subsequently, 50 μL of each sample was transferred to a 96-well plate, and 200 μL of the prepared zinc reaction reagent was added to each sample. The samples were incubated at room temperature for 10 min and measured at OD560nm using a CLARIOstar Plus microplate reader (BMG Labtech). For intracellular zinc (ab241014) measurements, cells were harvested and washed twice with 1 mL of chilled 1X assay buffer. The pellet was resuspended in 1 mL of 1X Assay Buffer, and 2 μL of Zinc Probe (500X) was added to the 1 mL cell suspension. The cells were then incubated at 37°C with 5% CO_2 for 30 min. After removing the stain and washing the cells twice with 1X Assay Buffer, the cells were resuspended in 1 mL of 1X Assay Buffer, and analyzed by flow cytometry (NovoCyte Quanteon, Agilent).

QUANTIFICATION AND STATISTICAL ANALYSIS

The results were reported as mean ± standard deviation (SD), as described in the figure legends. Plots were created using GraphPad Prism 10 and IBM SPSS Statistics 22. Violin plots were shown as kernel density estimations (KDE) with median values ± IQR. *p* values were determined using the two-sided unpaired t-test. scRNA-seq analysis were assessed using the two-sided Wilcoxon signed-rank test or Kruskal-Wallis one-way analysis of variance. Gene correlation coefficients (r) were calculated through two-sided Pearson and Spearman correlation analysis. The prognostic relevance of SOX4 and ZIP14 in progression-free survival was assessed using the Kaplan-Meier method, with statistical significance determined by the Log rank test. *p* values equal to or less than 0.05 were considered statistically significant. Each experiment was independently replicated at least three times.